ISSN: •2708-6437(Online)
•2708-6429(Print)

Journal of
Engineering Advancements

Editor-in-Chief:
Prof. Dr. Mohammad Mashud

Volume 05 Issue 01

SciEn

Published by:
SciEn Publishing Group

Journal of Engineering Advancements
Apt. # 6 C-D, House # 191
Road # 12/A, Dhanmondi R/A
Dhaka-1209, Bangladesh
Email: jea@scienpg.com Website: www.scienpg.com/jea/

SciEn
Published in: March 2024
Published by: SciEn Publishing Group
Price: Each Issue BDT 200.00 (US$ 15) **ISSN:** 2708-6437 (Online) 2708-6429 (Print)

Journal of Engineering Advancements
Apt. # 6 C-D, House # 191
Road # 12/A, Dhanmondi R/A
Dhaka-1209, Bangladesh
Email: jea@scienpg.com Website: www.scienpg.com/jea/

Journal of Engineering Advancements

Volume 05, Issue 01 March 2024

CONTENTS

Original Articles

Journal of
Engineering Advancements

Published by: SciEn Publishing Group

Apt. # 6 C-D, House # 191, Road # 12/A
Dhanmondi, Dhaka-1209, Bangladesh
Email Address: jea@scienpg.com

www.scienpg.com/jea/

This page is left intentionally blank

SciEn
Journal of Engineering Advancements Vol. 05(01) 2024, pp 1-8 https://doi.org/10.38032/jea.2024.01.001

Numerical Analysis of Laminar Natural Convection Inside Enclosed Squared and Trapezoidal Cavities at Different Inclination Angles

Mohammad Sultan Mahmud, Md. Mahbubur Rahman, Md. Nahid Zaman Liton*

Department of Mechanical Engineering, Khulna University of Engineering & Technology, Khulna-9203, Bangladesh

Received: November 27, 2023, Revised: January 08, 2024, Accepted: January 16, 2024, Available Online: January 19, 2024

ABSTRACT

The effects of cavity shape by inclination angle on laminar natural convection inside trapezoidal and square-shaped cavities have been numerically investigated in this work. Several simulations had been conducted for various inclinations of the trapezoidal cavity at Rayleigh numbers (Ra) $=10^5$ to 10^6 in a laminar flow regime. The walls at the left and right sides of the cavities were heated isothermally, while the walls at the top and bottom sides were adiabatic. The problem was assumed to be 2-D and solved using the software package ANSYS Fluent 16.2. Cavity filled with air is examined in two distinct instances; varying boundary layers and the flow generated for the natural convection. This numerical study analyzed the flow characteristics, temperature distribution, and Nusselt number. The analysis reveals that as the Rayleigh number increases, the Nusselt number also increases, with a more pronounced effect at higher Rayleigh numbers. It has been observed that there is a substantial effect of cavity shapes on the Nusselt number. The presence of an angled wall inhibits convection resulting in stronger flow in the squared cavity compared to the trapezoidal cavity. From numerical results, it is also found that the temperature distribution at Ra = 10^5 is wider than the temperature distribution at Ra= 10^6.

Keywords: Natural Convection, Nusselt Number, Inclination Angle, Rayleigh Number, Laminar Flow.

1 Introduction

A specific type of flow known as natural convection occurs when a fluid, like air, moves across space because some of its constituent parts are heavier than others rather than because of external forces. Buoyancy is the driving force for free convection. Free convection occurs when a fluid encompassing a heat source absorbs heat and then becomes less dense and rises because of thermal expansion. Thermal expansion that is caused in the fluid is critical. In other words, a heavier component results in less dense components falling, while lighter components result in more dense components rising, resulting in bulk fluid movement.

Researchers are becoming highly interested in natural convection in enclosures because of its wide range of applications and significant influence on thermal characteristics. Since natural convection is employed in a wide range of technical applications, including geophysics, geothermal reservoirs, building insulation, industrial separation processes, and so forth, it has been studied inside a variety of enclosure shapes and with a variety of boundary conditions to investigate thermal behavior as well as fluid flow. In many engineering systems, as well as geophysical situations when the enclosure geometry fluctuates or has additional tending walls, any triangle, square, or rectangular hole is unsuitable. Because of the slanted walls, examining natural convection in a trapezoidal enclosure is significantly more challenging than in any other enclosure.

Some parameters, such as the enclosure's shapes, angle of inclination, aspect ratio, and Rayleigh number, govern natural heat transport characteristics inside the enclosures. An extensive investigation was carried out to determine the influence of enclosure Rayleigh number and aspect ratio. Adibi *et al.* [1] and De Vahl Davis [2] investigated the heat transport properties of a 2-D rectangular and trapezoidal enclosure with isothermal boundary conditions for various Rayleigh number and aspect ratios by using numerical methods. When the Rayleigh number exceeds specific threshold values, the fluid flow becomes turbulent because of the induced buoyancy. Sharif and Liu [3] investigated how various inclination angles affected turbulent convection in rectangular-shaped cavities. In two separate studies, Adibi and Razavi [4], [5] simulated spontaneous and forced convection in three different bench markings. The author's benchmarks were flow over a cylinder that is round and flow through a squared cavity, which is comprised of two parallel plates. They employed an innovative numbering scheme that they came up with on their own. Heat transport was studied numerically and experimentally by Akbari [6]. For numerical simulations, he used the finite difference method. Zaharudddin *et al.* [7] numerically investigated the natural convection driven by buoyancy and Marangoni effects within a right-angled trapezoidal-shaped cavity containing water-based nanofluids. Alshomrani *et al.* [8] investigated the effect of the cooler's placement, aspect ratio, and positioning of the heated solid object within the enclosure numerically on the three-dimensional natural convection flow. Yazdani *et al.* [9] carried out a computational analysis on an enclosure of a trapezoidal shape filled with a non-Newtonian fluid following a power-law behavior. Their study focused on heat transfer by natural convection within the enclosure and the resulting generation of entropy. Mote Gowda *et al.* [10] explored free convection within a trapezoidal-shaped enclosure featuring discrete heating. Reddy *et al.* [11] studied extensively the heat transfer phenomenon by natural convection originating from a heated cylinder positioned within a square-shaped cavity containing micro-polar fluid. Kishor *et al.* [12] conducted both numerical simulation and experimental work in vertically oriented closed cavities for an aspect ratio of three, utilizing air as the working fluid at various

*Corresponding Author Email Address: sultan@me.kuet.ac.bd Published by: SciEn Publishing Group

temperature differences and Rayleigh numbers. Inam [13] investigated laminar natural convection in a square-shaped cavity at various inclination angles by direct numerical simulation. Ghalambaj *et al.* [14] explored the conjugate natural convection phenomenon within a square-shaped cavity using nanofluid while varying the volume fraction of the nanoparticles at different Rayleigh numbers and thermal conductivity ratio between wall and nanofluid. Nadim *et al.* [15] also performed a numerical investigation in a rectangular enclosure with a rotating object inside for a comprehensive analysis of fluid flow inside the field.

From the earlier literature review, it is observed that there is a less amount of research work on the effect of inclination angle (φ=0˚, φ=45˚, φ=50˚ and φ=60˚) of a trapezoidal-shaped cavity at considerably low Rayleigh number which was the motivation for current research work. Several simulations were performed for different inclination angles of a trapezoidal-shaped cavity at two Rayleigh numbers Ra = 10^5 and Ra = 10^6 using ANSYS Fluent 16.2. Natural convection in both trapezoid and squared-shaped cavities has been simulated in this work using numerical methods under various conditions. In this work, different geometry and different boundary conditions are examined, and results for these different conditions have been analyzed.

2 Methodology

The physical system of the problem has been illustrated in Fig. 1.

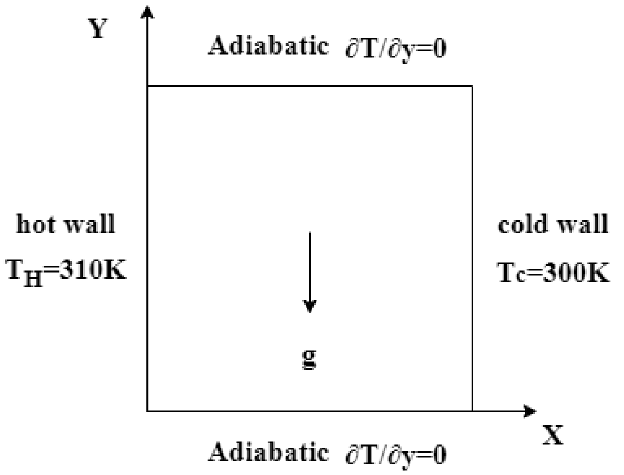

(a)

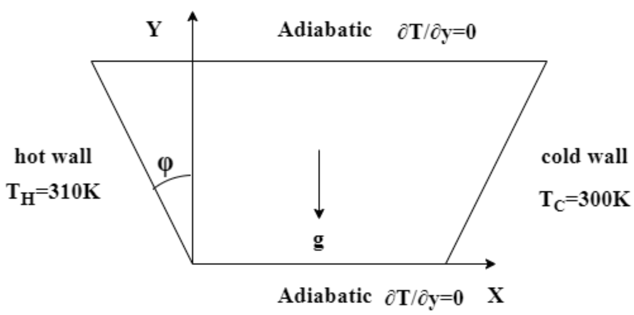

(b)

Fig. 1 Schematic diagram of the physical system for enclosed (a) square (φ=0˚) and (b) trapezoid (φ>0˚) cavities

This study considers two separate states. In the first case, the original environment is created in a squared-shaped cavity (φ=0˚). In this situation, the fluid in the cavity is termed air applied to the equation of state as the gas equation. The second case possesses similarity to the first one, but the shape of the cavity is trapezoidal (φ>0˚). Air is used as fluid inside the trapezoidal cavities in this case. Different angles of inclination (φ=45˚ to 60˚) at both sides of the cavities were used for simulation to monitor how the inclination angle affects the natural convection in the trapezoidal cavities. The temperature of the right cold wall is 300K, whereas the temperature of the left hot wall is 310K. The upper and lower walls were set adiabatic i.e. $\frac{\partial T}{\partial y} = 0$.

The numerical domain used for simulation was a two-dimensional square and trapezoid cavity with dimensions 200mm x 200mm containing air sketched in Fig. 2. The walls at the top and the bottom sides were set adiabatic, the slope of the trapezoid cavities has been changed. The Boussinesq approximation used for relating the temperature field to the flow field in the motion has been applied for simplifying the calculations of buoyancy due to density difference in the current study of natural convection heat transfer.

(a)

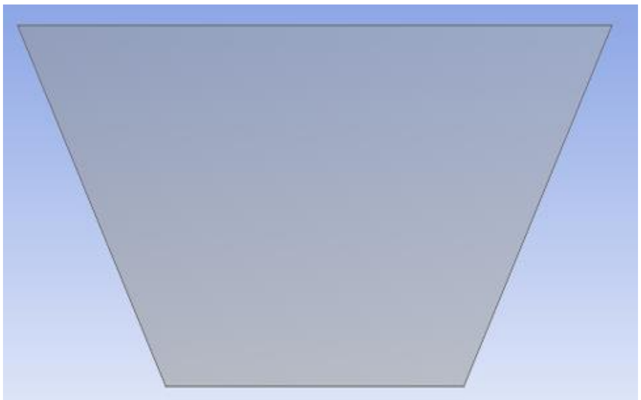

(b)

Fig. 2 Computational domain of (a) squared and (b) trapezoidal cavities for numerical simulation.

Fig. 3 shows the grids that were considered for the square and trapezoid. Because created boundary layers necessitate high-accuracy computations, the grids positioned alongside the walls are finer than those at locations further away from the walls.

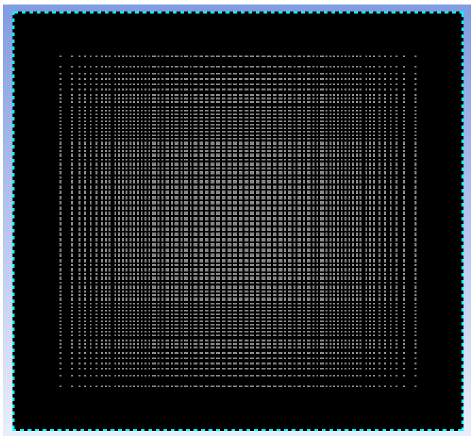

(a)

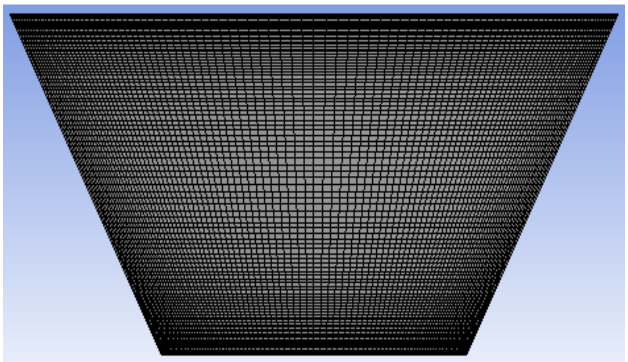

(b)

Fig. 3 Grid for (a) squared and (b) trapezoid cavities

The face sizing and edge sizing procedures are used to create the mesh. The grid size used in this simulation is 150x150. For better results of thermal performance, the meshing was done by using bias. For biasing, a bias factor value of 5 was used. Fig. 4 represents the mesh independency test result for the trapezoid cavities.

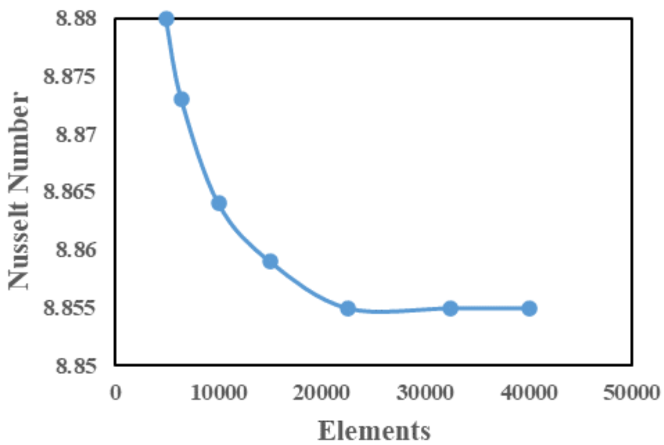

Fig. 4 Mesh independence test for the simulation work

In heat transfer at a boundary (surface) within a fluid, the Nusselt number (Nu) is the ratio of convective to conductive heat transfer across (normal to) the boundary.

$$Nu = \frac{Convective\ heat\ transfer}{conductive\ heat\ transfer} = \frac{h\,L}{k} \tag{1}$$

Where h is the convective heat transfer coefficient of the flow, L is the characteristic length, and k is the thermal conductivity of the fluid.

The Rayleigh number is a dimensionless number that is associated with buoyancy-driven airflow and can be regarded as a measure of the driving forces of natural convection.

Thus, the Rayleigh number is defined as

$$Ra = \frac{g\beta\rho^2 C_p \Delta T L^3}{\mu k} \tag{2}$$

Where g is the acceleration of gravity, β is the thermal expansion coefficient, ρ is the density of the fluid, ΔT is the temperature difference, L is the length of the enclosure, μ is dynamic viscosity and k is the thermal conductivity.

The progression of natural convection flows within the enclosure is governed by the following set of governing equations [16] using the Boussinesq approximation [17].

$$\frac{\partial u}{\partial x} + \frac{\partial v}{\partial y} = 0 \tag{3}$$

$$u\frac{\partial u}{\partial x} + v\frac{\partial u}{\partial y} = \frac{1}{\rho} - \frac{\partial P}{\partial X} + \left(\frac{\partial^2 u}{\partial x^2} + \frac{\partial^2 u}{\partial y^2}\right) \tag{4}$$

$$u\frac{\partial v}{\partial X} + v\frac{\partial v}{\partial y} = -\frac{1}{\rho}\frac{\partial P}{\partial y} + \left(\frac{\partial^2 v}{\partial x^2} + \frac{\partial^2 v}{\partial y^2}\right) + g\beta + (T - T_o) \tag{5}$$

$$u\frac{\partial T}{\partial x} + v\frac{\partial T}{\partial y} = k\left(\frac{\partial^2 T}{\partial x^2} + \frac{\partial^2 T}{\partial x^2}\right) \tag{6}$$

where u, v are the velocity components in the x and y direction, respectively. ρ is the density of air. Also, ϑ and k are kinematic viscosity and thermal diffusivity respectively. The volumetric thermal expansion coefficient is denoted by β and g represents the acceleration of gravity. The above equations (Eq. (3) to Eq. (6)) are numerically solved using the technique of finite volume method. The appropriate boundary conditions of the problem are:

For left wall: $u = v = 0$ & $T_H = 310K$

For right wall: $u = v = 0$ & $T_C = 300K$

For lower and upper walls: $u = v = 0$ & $\frac{\partial T}{\partial y} = 0$

The geometric models are solved by using ANSYS Fluent 16.2. For the residuals, the convergence criteria are set to10^{-8} for the continuity equation, x-velocity and y-velocity equation, and energy equation. In solution initialization, the standard initialization approach was used, and solution initialization is necessary before the computation executes. It was repeated until the convergence requirements were met.

As indicated in Table 1, the current numerical simulation has been validated against solutions found in the literature. The average Nusselt number at the hot wall of the air-filled square cavity, as determined by many investigations, is displayed in Table 1 and contrasted with the results of the current investigation for varying Rayleigh numbers.

The Rayleigh number ranged from 10^3 to 10^6 in the laminar flow regime (a flow regime characterized by high momentum diffusion and low momentum convection) have been considered in the current analysis.

Table 1 Comparison of Nusselt number at the hot wall of the square cavity of the current work with previous works

Rayleigh Number	Present study	Vahl Davis and Jones [18]	Fusegi et al. [19]	Khanafer et al. [20]	Billigen [21]	Lai and Yang [22]	Kobra et al. [23]
10^3	1.1179	1.118	1.105	1.118	-	1.126	-
10^4	2.247	2.243	2.302	2.245	2.245	2.252	2.2448
10^5	4.534	4.519	4.646	4.522	4.521	4.514	4.5216
10^6	8.855	8.799	9.012	8.826	8.800	8.752	8.8262

3 Results and Discussion

Fig. 5 shows the contour showing the temperature of trapezoidal cavities for different shapes of geometry and for variation of inclination angle at Rayleigh number 10^6. Fig. 5(a) depicts the temperature of trapezoid cavities for different angles $\varphi = 45^\circ$, $\varphi = 50^\circ$, $\varphi = 60^\circ$ respectively at Rayleigh number 10^6. From all the figures, it is seen that the temperature close to the left wall is higher than the right wall. It is due to the higher temperature of the wall at the left which is 310K than the wall at the right which is 300K.

It is also seen that the temperature at the wall of the top side is larger than the temperature at the wall of the bottom side. It is because the temperature of the fluid close to the left wall is raised because of heating. Consequently, fluid density decreases. Then this warm air travels to the top wall which results in higher temperature near the top wall than the bottom wall. Again, the temperature close to the right wall is lower than the left wall because of buoyancy. For the cooling effect, fluid density increases near the right wall, and fluid becomes heavier and colder near the right wall. A similar observation was found in other open literature [13].

Fig. 6 illustrates the contour showing the temperature of trapezoid cavities for different shapes of geometry and for variation of inclination angle at Rayleigh number 10^5.

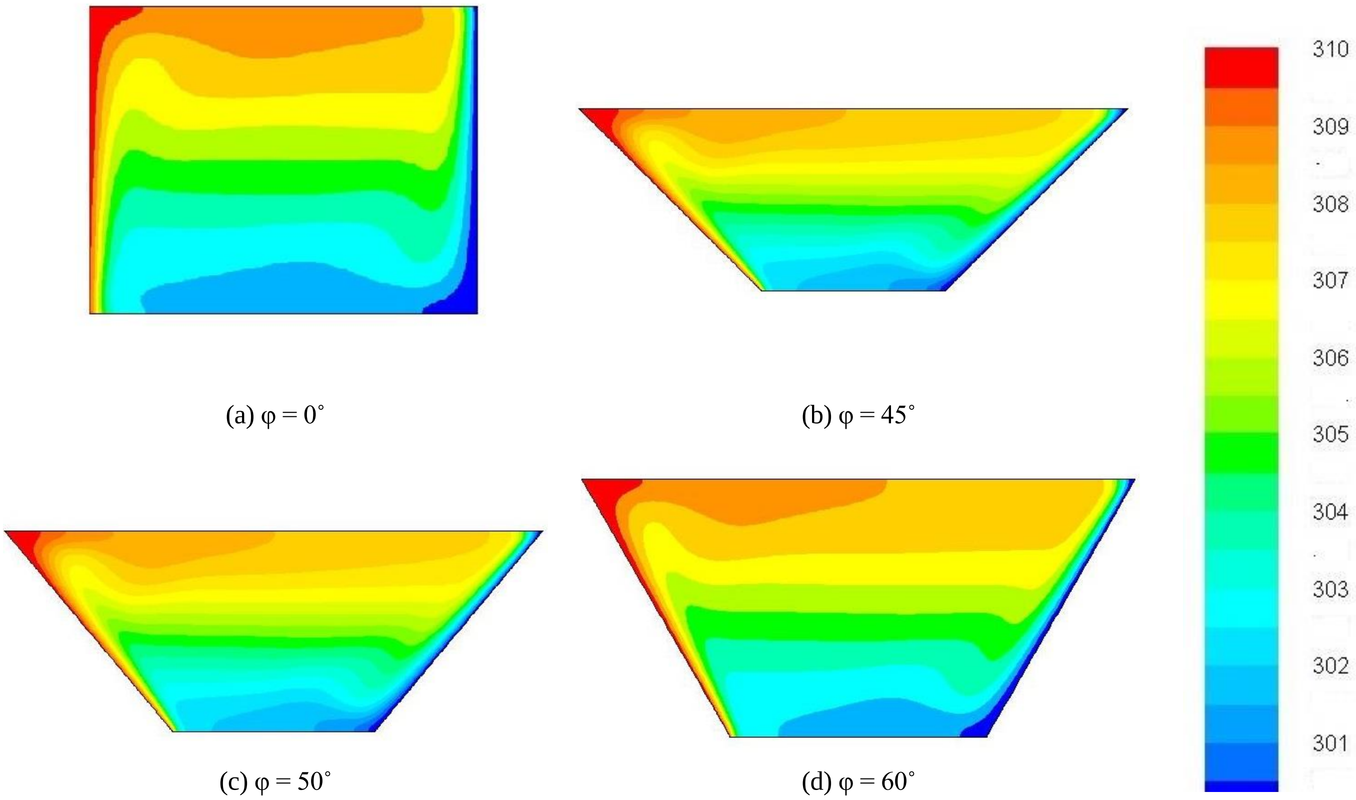

(a) $\varphi = 0^\circ$

(b) $\varphi = 45^\circ$

(c) $\varphi = 50^\circ$

(d) $\varphi = 60^\circ$

Fig. 5 Contour of the temperature of the square and trapezoid cavities for different inclination angles φ of (a) 0˚, (b) 45˚,(c) 50˚ and (d) 60˚at Ra = 10^6

.

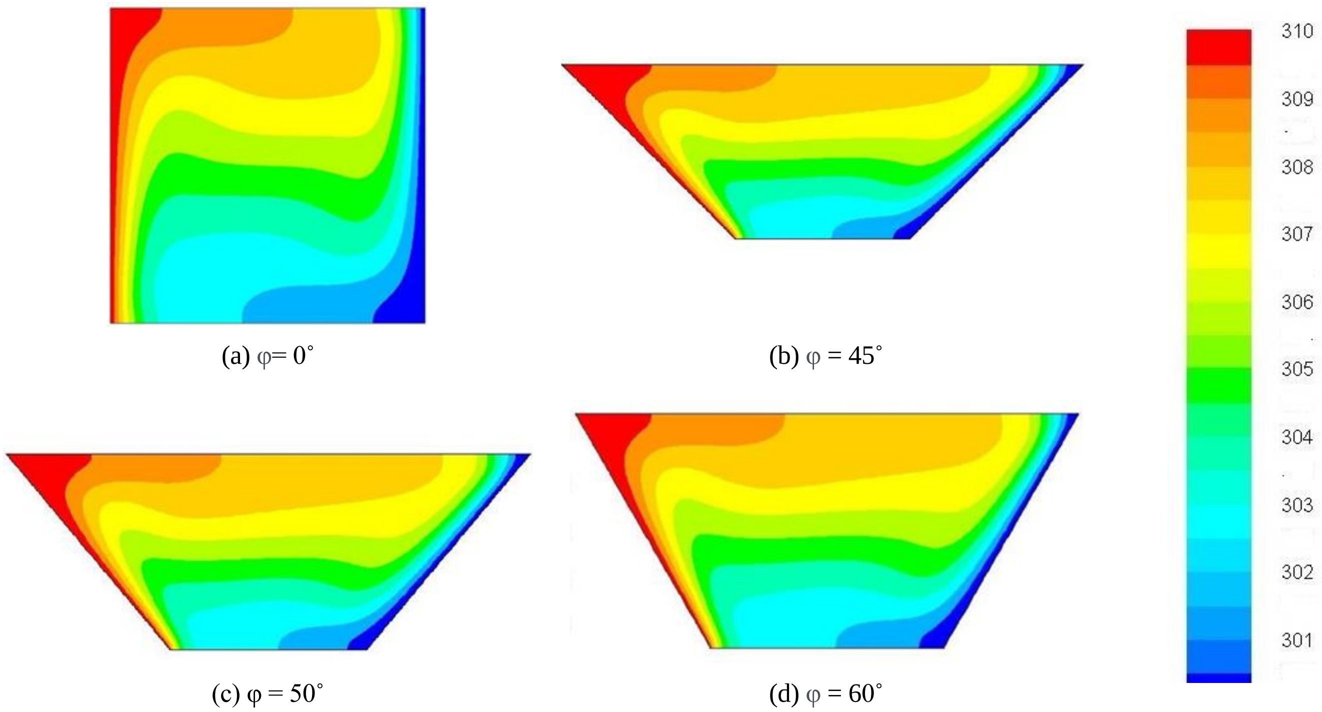

(a) φ= 0˚ (b) φ = 45˚

(c) φ = 50˚ (d) φ = 60˚

Fig. 6 Contour of the temperature of the square and trapezoid cavities for different inclination angles φ of (a) 0˚, (b) 45˚,(c) 50˚ and (d) 60˚ at Ra = 10^5

Fig. 6(a) discusses the temperature of the square cavity (φ= 0˚) at Rayleigh number 10^5. Fig. 6(b), (c), and (d) show the temperature of trapezoid cavities of different angles φ= 45˚, φ=50˚, φ=60˚ respectively at Rayleigh number 10^5. It is seen that the temperature close to the left wall is higher than the right wall. It is due to the higher temperature of the wall at the left which is 310K than the wall at the right which is 300K. From all the figures, it is also observed that the temperature of the top wall is higher than the temperature of the bottom wall. It is because the temperature of the fluid near the left wall raised because of heating. Hence, fluid density decreases. Then this warm air travels to the top wall which results in higher temperature near the top wall than the bottom wall. Again, the temperature near the right wall is lower than the left wall due to the buoyancy effect. For the cooling effect, fluid density increases near the right wall, and fluid becomes heavier and colder near the right wall. From Fig. 5 and Fig. 6, it is observed that the temperature distribution at Rayleigh number 10^5 is more elongated than the temperature distribution at Rayleigh number 10^6.

Fig. 7 shows how the Nusselt number at the hot wall of the cavities varies with the Rayleigh number for different shapes and different inclination angles. Analysis of Fig. 7(a) reveals intriguing trends in Nusselt numbers concerning squared and trapezoid (φ = 50˚) cavities. Initially, at low Rayleigh numbers, both cavities exhibit little variations. However, with rising Rayleigh numbers, a distinctive shift occurs, causing a monotonic increase in Nusselt numbers for both shapes. As the Rayleigh number escalates further, a marked and considerable upsurge in the Nusselt numbers is observed. For instance, at a Rayleigh number of 10^3, the Nusselt number for the squared cavity is 1.1179, significantly lower than 8.8558 at 10^6. Similarly, for the trapezoid cavity, the Nusselt number climbs from 1.4771 at Ra=10^3 to 15.889 at Ra=10^6, signifying a notable increment. Remarkably, comparisons between the two cavities at identical Rayleigh numbers reveal the trapezoid cavity consistently yielding higher Nusselt numbers.

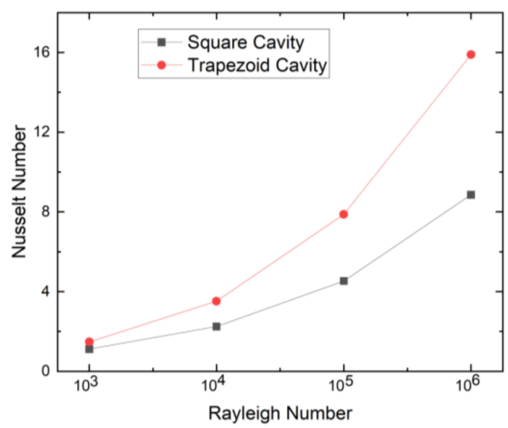

(a)

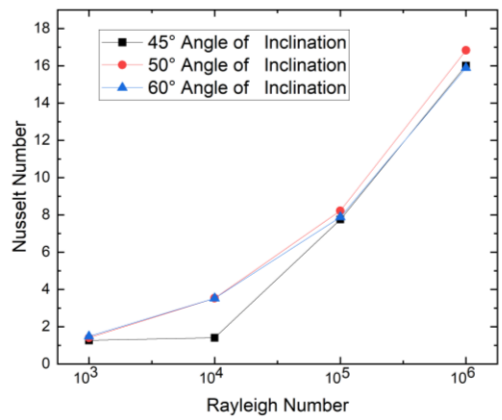

(b)

Fig. 7 Variation of Nusselt number with Rayleigh number for (a) different shape and (b) varying angle of inclination in trapezoid cavities

At lower Rayleigh numbers, the Nusselt number difference between the squared and trapezoid cavities is marginal but becomes more pronounced as the Rayleigh number increases.

Fig. 7(b) demonstrates how the angle of inclination affects the Nusselt number's behavior across different Rayleigh numbers. From the data the Nusselt number changes depending on the slope of the surface. At inclination angles φ =60˚ and φ =50˚, there's a similar trend in how the Nusselt number changes with increasing Rayleigh numbers. Initially, at lower Rayleigh numbers (Ra= 10^4 to 10^5), the Nusselt number grows slowly, but this increase becomes much more pronounced at higher Rayleigh numbers of Ra=10^5 to 10^6. However, at an inclination angle of φ=45˚, the behavior of the Nusselt number is distinct from that observed at φ=60˚ and φ=50˚ at Ra=10^4. Specifically, at φ=50˚, the Nusselt number surpasses both φ=60˚ and φ=45˚ angles, indicating a better heat transfer efficiency. Hence, the enclosed trapezoid shape cavity with the inclination angle of φ=50˚ is the optimum consideration for laminar natural convection among the selection of the angles in the current study.

Fig. 8 and Fig. 9 explain velocity contour for squared and trapezoid cavities at Rayleigh number Ra = 10^6 and Ra = 10^5 respectively. In Fig. 8 and Fig. 9, the velocity varies with position inside the squared and trapezoid cavities. For the heating and cooling effects of natural convection, low-dense fluids move toward the top wall from the bottom wall and high-dense fluids move toward the top wall to the bottom wall respectively. From the numerical result, it is found that there is variation in velocity for different positions inside the trapezoid cavity due to the behavior of natural convection. As the Rayleigh number increases, velocity increases significantly. At a low Rayleigh number, velocity remains very low due to the behavior of natural convection. Velocity inside the cavity is created by some parts of the air being heavier than others. Due to the high temperature of the left wall, there occurs heating. For heating, the density of air near the left wall decreased. The air with reduced density moves relatively faster than the other air inside the cavity. Similarly, near the right wall, there occurs a cooling process. As a result, the air is heavier than the others in this region. Then, this heavier air moves down towards the bottom wall. For this density variation, velocity varies inside the cavity.

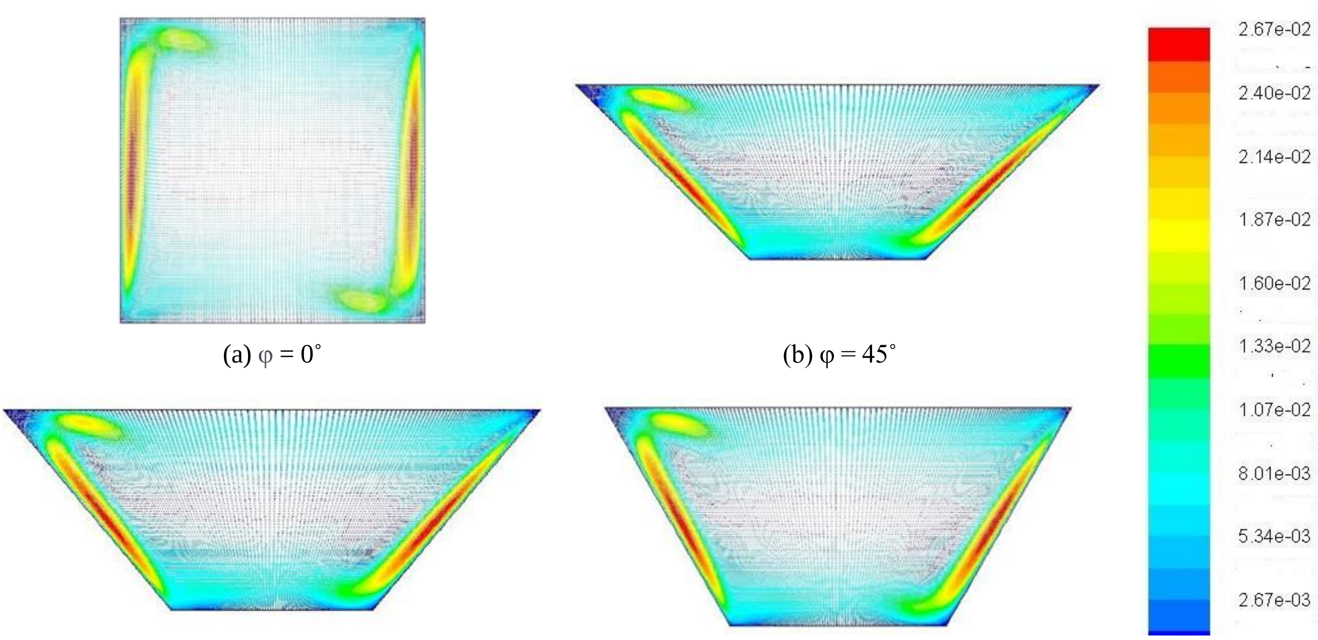

(a) φ = 0˚ (b) φ = 45˚ (c) φ = 50˚ (d) φ = 60˚

Fig. 8 Velocity contour of the square and trapezoid cavities for different inclination angle φ of (a) =0˚, (b) 45˚, (c) 50˚ and (d) 60˚at Ra = 10^6

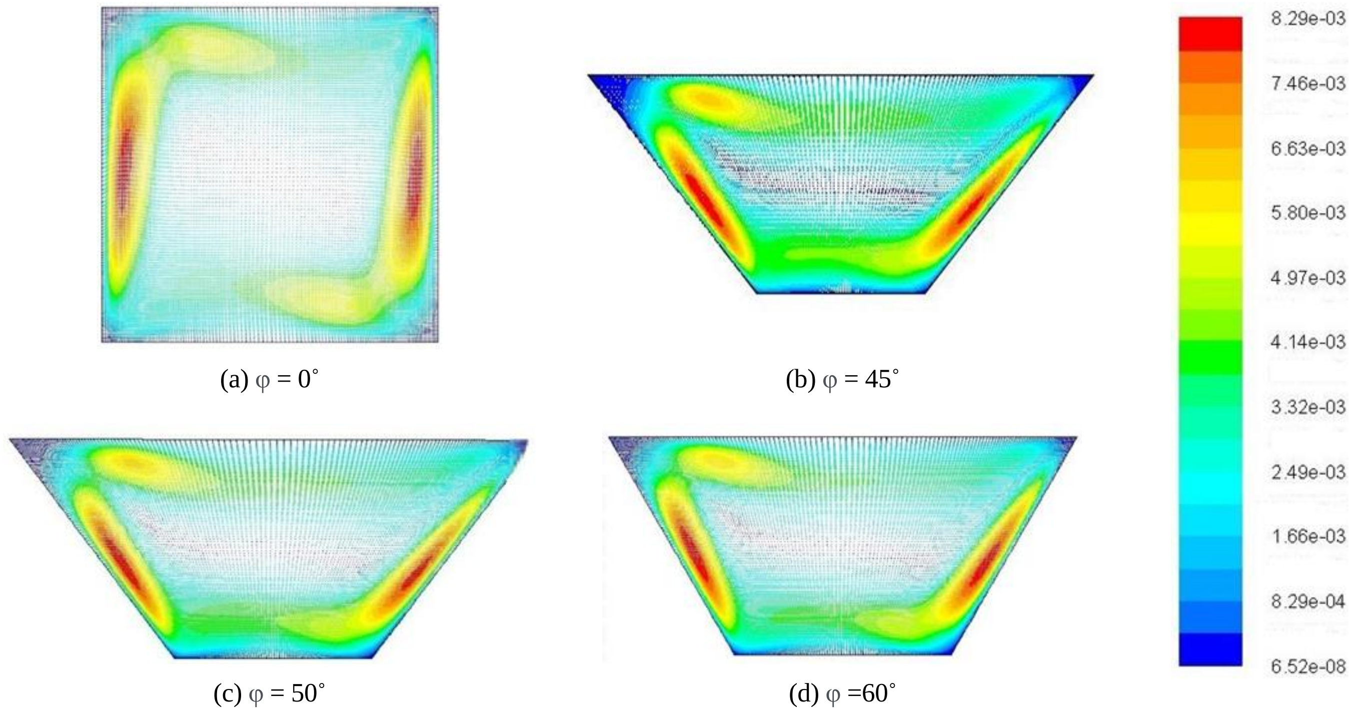

Fig. 9 Velocity contour of the square and trapezoid cavities for different inclination angles φ of (a) =0˚, (b) 45˚, (c) 50˚ and (d) 60˚ at Ra = 10^5

It is observed that points adjacent to the wall have the highest value because of the behavior of natural convection. In the points near the wall, heating and cooling occur. Heating occurs in the left wall, whose temperature is higher than that of the right wall. Due to high temperature, fluids take heat and become less dense. For variation in density, fluids with reduced density travel more quickly. Hence, in these points, fluids gain more velocity. Furthermore, at points far from walls, there is a lack of heat source for varying the density. So, inside the cavity at points far from the wall (almost in the middle of the cavities) fluids move less or none. Therefore, velocity becomes near to zero.

4 Conclusions

Different geometries for different shapes such as squared and trapezoid cavities and for different angles of inclination were analyzed numerically under natural convection conditions in this research. Four geometries were taken for study and numerically analyzed. The Nusselt number was measured, for all the geometries for both squared cavity and trapezoid cavity for various angles of inclination. From the result of the work, it is observed that the Nusselt number varies nonlinearly with the Rayleigh number. Nusselt number changes slowly at a low Ra number whereas the Nusselt number increases significantly and at a faster rate at a high Rayleigh number. The Nusselt number is also significantly affected by the shape of geometries. The Nusselt numbers for the trapezoid cavity are larger than the Nusselt numbers for the squared cavity at the same Rayleigh number. From numerical results, it is found that the temperature distribution at Ra = 10^5 is wider than the temperature distribution at R = 10^6. The velocity contours demonstrated the behavior of natural convection, showing zero velocity at the walls and higher velocity near the heated wall due to density variations. When compared to trapezoid cavities, the produced flow in the squared cavity is stronger due to the presence of an inclined wall inhibiting natural convection. Overall, these findings emphasize the significant impact of surface inclination on heat transfer efficiency, revealing diverse Nusselt number behaviors across different angles and Rayleigh numbers. Understanding these relationships is crucial for optimizing heat transfer in engineering and natural systems where inclined surfaces are involved.

Nomenclature

Symbols	Meaning	Unit
T_H	Hot wall Temperature	[K]
T_C	Cold wall Temperature	[K]
g	Acceleration of gravity	[m/s^2]
Ra	Rayleigh number	[–]
k	Thermal conductivity	[W/m-K]
h	Convective heat transfer coefficient	[W/m^{2}K]
Nu	Nusselt number	[–]
α	Thermal diffusivity	[m^2/s]
β	Volumetric thermal expansion coefficient	[1/K]
ρ	Density	[kg/m^3]
υ	Kinematic viscosity	[m^2/s]
φ	Angle of inclination	[˚]
X, Y	Cartesian coordinates	[m]
p	Pressure	[Pa]
ρ	Absolute density of air	[kg/m^3]

References

[1] Adibi, T., Kangarluei, R.A. and Farhangmehr, V., 2017. Numerical study of natural convection flow inside squared and trapezoidal cavities in various conditions. *International Journal of Science, Engineering and Technology Research*, *6*(5), pp.2278-2298.

[2] de Vahl Davis, G., 1968. Laminar natural convection in an enclosed rectangular cavity. *International Journal of Heat and Mass Transfer*, *11*(11), pp.1675-1693.

[3] Sharif, M.A.R. and Liu, W., 2003. Numerical study of turbulent natural convection in a side-heated square cavity at various inclination angles. *Numerical Heat Transfer: Part A: Applications*, *43*(7), pp.693-716.

[4] Adibi, T. and Razavi, S.E., 2015. A new characteristic approach for incompressible thermo-flow in Cartesian and non-Cartesian grids. *International Journal for Numerical Methods in Fluids*, *79*(8), pp.371-393.

[5] Razavi, S.E. and Adibi, T., 2016. A novel multidimensional characteristic modeling of incompressible convective heat transfer. *Journal of Applied Fluid Mechanics*, *9*(3), pp.1135-1146.

[6] Akbari Kangarluei, R., 2015. Heat and mass transfer in industrial biscuit baking oven and effect of temperature on baking time. *Journal of Heat and Mass Transfer Research*, *2*(2), pp.79-90.

[7] Zaharuddin, S.D.A.S., Siri, Z., Saleh, H. and Hashim, I., 2020. Buoyant Marangoni convection of nanofluids in the right-angled trapezoidal cavity. *Numerical Heat Transfer, Part A: Applications*, *78*(11), pp.656-673.

[8] Alshomrani, A.S., Sivasankaran, S., Amer, A.A. and Biswas, A., 2019. Numerical study on convective flow in a three-dimensional enclosure with hot solid body and discrete cooling. *Numerical Heat Transfer, Part A: Applications*, *76*(2), pp.87-99.

[9] Yazdani, K., Sahebjamei, M. and Ahmadpour, A., 2019. Natural convection heat transfer and entropy generation in a porous trapezoidal enclosure saturated with power-law non-Newtonian fluids. *Heat Transfer Engineering, 41*(11), pp. 982-1001.

[10] Gowda, K.G.B.M., Rajagopal, M.S. and Seethramu, K.N., 2019. Numerical studies on natural convection in a trapezoidal enclosure with discrete heating. *Heat Transfer Engineering, 41*(16), pp. 1-12.

[11] Sivarami Reddy, C., Ramachandra Prasad, V. and Jayalakshmi, K., 2021. Numerical simulation of natural convection heat transfer from a heated square cylinder in a square cavity filled with micropolar fluid. *Heat Transfer*, *50*(6), pp.5267-5285.

[12] Kishor, V., Singh, S. and Srivastava, A., 2018. Investigation of convective heat transfer phenomena in differentially-heated vertical closed cavity: Whole field experiments and numerical simulations. *Experimental Thermal and Fluid Science*, *99*, pp.71-84.

[13] Inam, M.I., 2020. Direct numerical simulation of laminar natural convection in a square cavity at different inclination angle. *Journal of Engineering Advancements*, *1*(01), pp.23-27.

[14] Ghalambaz, M., Doostani, A., Izadpanahi, E. and Chamkha, A.J., 2020. Conjugate natural convection flow of Ag–MgO/water hybrid nanofluid in a square cavity. *Journal of Thermal Analysis and Calorimetry*, *139*, pp.2321-2336.

[15] Nadeem, S., Haider, J.A., Akhtar, S. and Ali, S., 2022. Numerical simulations of convective heat transfer of a viscous fluid inside a rectangular cavity with heated rotating obstacles. *International Journal of Modern Physics B*, *36*(28), p.2250200.

[16] Saleh, H., Roslan, R. and Hashim, I., 2011. Natural convection heat transfer in a nanofluid-filled trapezoidal enclosure. *International Journal of Heat and Mass Transfer*, *54*(1-3), pp.194-201.

[17] Saha, S.C., Patterson, J.C. and Lei, C., 2010. Natural convection in attics subject to instantaneous and ramp cooling boundary conditions. *Energy and Buildings*, *42*(8), pp.1192-1204.

[18] de Vahl Davis, G. and Jones, I., 1983. Natural convection in a square cavity: a comparison exercise. *International Journal for Numerical Methods in Fluids*, *3*(3), pp.227-248.

[19] Fusegi, T., Hyun, J.M., Kuwahara, K. and Farouk, B., 1991. A numerical study of three-dimensional natural convection in a differentially heated cubical enclosure. *International Journal of Heat and Mass Transfer*, *34*(6), pp.1543-1557.

[20] Khanafer, K., Vafai, K. and Lightstone, M., 2003. Buoyancy-driven heat transfer enhancement in a two-dimensional enclosure utilizing nanofluids. *International Journal of Heat and Mass Transfer*, *46*(19), pp.3639-3653.

[21] Bilgen, E., 2005. Natural convection in cavities with a thin fin on the hot wall. *International Journal of Heat and Mass Transfer*, *48*(17), pp.3493-3505.

[22] Lai, F.H. and Yang, Y.T., 2011. Lattice Boltzmann simulation of natural convection heat transfer of Al2O3/water nanofluids in a square enclosure. *International Journal of Thermal Sciences*, *50*(10), pp.1930-1941.

[23] Kobra, F., Quddus, N. and Alim, M.A., 2014. Heat transfer enhancement of Cu-water nanofluid filled in a square cavity with a circular disk under a magnetic field. *Procedia Engineering*, *90*, pp.582-587.

SciEn
Journal of Engineering Advancements Vol. 05(01) 2024, pp 9-13 https://doi.org/10.38032/jea.2024.01.002

Performance of Ceramic Tiles Waste as a Partial Replacement of Brick Aggregate on Mechanical and Durability Properties of Concrete

Sumit Basak, Md. Rashedul Haque, Abul Kalam Azad, Md. Muntasir Rahman*

Department of Civil Engineering, Faculty of Engineering, Hajee Mohammad Danesh Science and Technology University (HSTU), Dinajpur-5200, Bangladesh

Received: November 19, 2023, Revised: February 06, 2024, Accepted: February 06, 2024, Available Online: February 21, 2024

ABSTRACT

The availability of natural aggregates such as stone chips is a particularly challenging issue nowadays. Ceramic materials are increasingly being used in new projects such as tiles, sanitary fittings, electrical insulators, and so on, due to ceramic's fragile properties, which often break during production, shipping, and installation. So, ceramic waste is one of these materials that are probably cost-efficient to use as a substitution (0%, 25%, 50%, and 75%) for brick chips. This research examined the mechanical strength properties of ceramic tile waste (CTW) concrete, including its compressive strength and splitting tensile strength, and utilized a water absorption test to assess its durability and performance. This research used a mix ratio of 1:1.5:3 with a constant water-cement ratio (w/c) of 0.45, and a water-reducing superplasticizer named Conplast SP337 was used. For the mechanical and durability tests, a total of seventy-two (72) concrete cylinders of 100 mm × 200 mm were cast, cured, and tested at 7, and 28 days. Mechanical strength results revealed a significant increase of around 16.71% for 50% CTW concrete mixtures at the place of brick aggregates, and the water absorption performance improved with the incorporation of CTW in concrete mixes.

Keywords: Ceramic Tiles Waste, Brick Chips, Superplasticizer, Mechanical Properties, Durability Properties.

1 Introduction

Concrete has been broadly recognized as a renowned construction material, basically because of its availability, affordability, performance, and comfort of working [1]. Concrete is a universally used construction material in all forms of structures. It is predicted that approximately 25,000 million tons of concrete will be produced annually. This equates to around 3.8 tons per person yearly [2]. For that reason, the natural resources of aggregates are depleting worldwide in the present day. Hence, it's possible that using substitute materials in place of natural aggregates will be necessary [3]. One of the most dangerous problems in the globe has been removing waste and reusing it. In several studies, researchers employed different waste materials as a substitution for natural aggregates in varying amounts and examined concrete's mechanical and durability aspects. Therefore, there is a growing concern for defending the atmosphere and a need to reserve natural resources, such as aggregate, by using complementary materials that are redundant as waste. Construction and demolition (C&D) wastes represent nearly 75% of all waste produced globally. Additionally, around 54% of the waste generated from construction as well as demolition is made up of waste from ceramic products [4], [5]. Ceramic items (tiles, electrical insulators, sanitary fittings, etc.) are increasingly being used in building and structural construction, owing to the fragile properties of ceramic, which often break during production, shipping, and installment. Ceramic waste, such as floor tiles, wall tiles, sanitary wares, as well as household ceramics, is probably cost-efficient to use as a substitution for natural aggregates [6]. Based on the global production data, China is the largest ceramic tile producer, producing 46.6% of the overall production, while India comes in third with 6.2% of the worldwide production [7], [8]. Over 12 billion m^2 of different kinds of ceramic tiles were produced worldwide in 2012. About thirty percent of the output in the ceramics sector is squandered [9], [10]. Ceramic aggregate has a low thermal expansion coefficient and is heat and abrasion-resistant. Additionally, ceramic items are very strong, long-lasting, and resistant to heat, fire, and wear. As such, using these industrial wastes in concrete in place of aggregates may prove to be a practical way to eliminate waste [11]-[14]. Many researchers have successfully attempted to build a basis for their future work by examining the mechanical properties of ceramic aggregate concrete [15]-[18] and the qualities of ceramic aggregate [19], [20]. The study on ceramic aggregate concrete needs to be compiled in an orderly manner to facilitate the use of ceramic wastes in structural concrete. This will help future researchers and potential builders by offering essential knowledge.

In Bangladesh, most of the construction works such as buildings, bridges, and highways are being constructed using a significant amount of local brick aggregates. The application of ceramic waste will lower the utilization of brick chips in concrete production. It will help control hazardous gases such as CO_2, CO, SO_2, NO_2, and others emitted from brickfields [21]. Utilizing ceramic waste tiles as a substitution for brick aggregate in concrete construction can have several potential implications, including environmental sustainability and cost-effectiveness. The objective of this research is to determine the safe proportion of ceramic waste aggregate (CWA) usage to improve the concrete without compromising its properties and to compare the mechanical properties such as compressive strength and splitting tensile strength between conventional brick aggregate concrete and CWA concrete. Besides these durability properties such as water absorption capacity will also be investigated in this research. Therefore, employing these

*Corresponding Author Email Address: rashed.civil@hstu.ac.bd

wastes in concrete manufacturing might be an efficient way to protect the environment while also increasing the quality of concrete.

2 Materials and Methodology

2.1 Materials

2.1.1 Cement

For this research, ordinary Portland cement (Premier cement) was utilized. It conforms to the Bangladesh Standard BDS EN 197-1:2003 CEM-I 42.5 N and 52.5 N.

2.1.2 Aggregates

Sand. River sand was used as fine aggregate in concrete. The origin of this sand was the Panchagarh district, which was collected from Dosmile in the Dinajpur district.

Brick chips. It's a coarse aggregate composed of broken bricks. Brick gravel, brick khoa, and brick ballast are its various names. For this research work, 19 mm downgrade brick chips were generally utilized as coarse aggregate. Sieve analysis was conducted for both sand, brick chips, and ceramic aggregate by ASTM standards.

Ceramic waste aggregate. This research used ceramic floor porcelain tiles as a Partial replacement for brick chips. Ceramic tile waste has been collected from Parbatipur, Dinajpur. The collected tiles were broken manually into standard aggregate sizes (19 mm downgrade). Fig. 1 shows the materials utilized in this research work.

(a) Cement

(b) Brick chips

(c) Sand

(d) Ceramic tile waste

(d) Ceramic tile aggregate

Fig. 1 Various types of materials used in this research work

2.1.3 Admixture

The main purpose of using admixture was to produce high-workability concrete without losing strength and high-quality concrete with improved durability. Conplast SP337 was used as a superplasticizer for the better workability of concrete, and a reduced water/cement ratio increased density.

2.1.4 Concreting ingredients

Concreting ingredients such as aggregate, cement, admixture, and water were collected locally and tested in various properties in the laboratory according to ASTM standards. Table 1 depicts the properties of aggregates.

Table 1 Properties of Aggregate

Property	Fine Aggregate (Sand)	Coarse Aggregate (Brick chips)	Ceramic Tile Aggregate	ASTM Standards
Fineness Modulus	3.16	6.16	6.96	ASTM C136 [22]
Maximum Aggregate Size (mm)	-	19	19	-
Unit Weight (kg/m^3)	1704	1130	1399	ASTM C29 [23]
Voids (%)	35.43	55.12	41.21	
Specific Gravity	2.65	1.80	2.39	ASTM C127 [24]
Water Absorption (%)	1.01	16.04	1.26	ASTM C128 [25]

2.2 Mix Proportions

A total of four mixes were prepared including the control mix containing brick chips. For conducting this research work, a mixed proportion of 1:1.5:3 was adopted, and a fixed w/c ratio of 0.45 for all mixes including the control mix was taken. A super-plasticizer admixture of 1% of the cementitious materials was used in all mixes to produce high-workability concrete without losing strength. The mixing proportions of concrete are summarized in Table 2.

Table 2 Mixing proportions of concrete

Mix Name	% of Broken Ceramic Tile Replacement	w/c Ratio	Cement (kg/m^3)	Water (kg/m^3)	Fine Aggregate (kg/m^3)	Brick Chips (kg/m^3)	CWT (kg/m^3)
CWA-0	0%	0.45	403	181.35	715.68	949.2	0
CWA-25	25%					711.9	237.3
CWA-50	50%					474.6	474.6
CWA-75	75%					237.3	711.9

2.3 Workability Test

This test was frequently used on construction sites across the world as an indirect measure of concrete performance. Finally, workability was examined at the end of each concrete mix according to standard ASTM C143 [26]. Fig. 2 shows the workability test of brick and CWA concrete.

Fig. 2 Workability test of brick and CWA concrete

2.4 Preparation of Concrete Specimen and Testing

A total of 24 nos of cylindrical concrete specimens (100 mm × 200 mm) were prepared and tested for mechanical properties such as compressive strength by ASTM C39 [27], 24 nos of specimens for split tensile strength by ASTM C496 [28], and 24 nos for durability properties such as water absorption tests. The test setup used in this research is shown in Fig. 3.

(a) Compressive strength setup

(b) Splitting tensile strength setup

Fig. 3 Compressive and splitting tensile strength setup

3 Results and Discussion

3.1 Workability

The slump value of conventional brick aggregate concrete was found to be 85 mm. After that, when the replacement was started at that time, the slump value increased. Because ceramic tile waste has a smooth surface, particles reduce friction and flow more easily. By replacing brick chips at a rate of 25%, 50%, and 75% with ceramic waste tiles, the slump value increases by about 41% for 75% of replacement of CWT than the 0% CWT. This increase in slump value is good for workability and ease of placement. Slump value of various mixes is shown in Fig. 4.

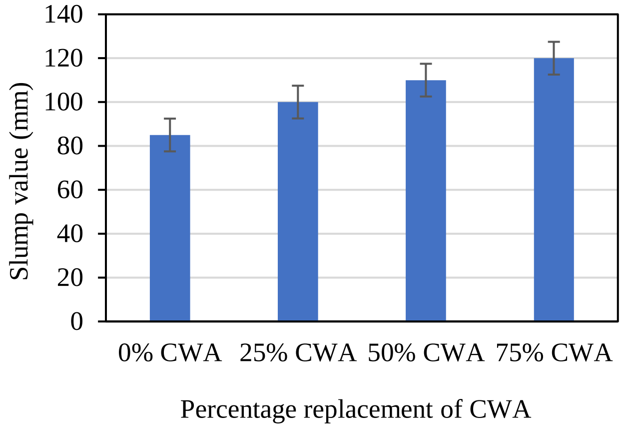

Fig. 4 Comparison of slump value of different concrete mixtures

3.2 Unit weight of Cylindrical Concrete Specimens

The unit weight of a cylindrical concrete specimen is the weight of the specimen per unit volume. In this research, unit weights for different types of mixed proportions were determined for brick and CWA concrete. Fig. 5 shows the comparison of the unit weight of brick and CWA concrete. The percent replacement of ceramic waste aggregate is increased the unit weight might be increased by around 9% for 75% replacement of CWT than 0% of CWT at 28 days because of higher specific gravity and lower presence of voids in ceramic waste aggregate.

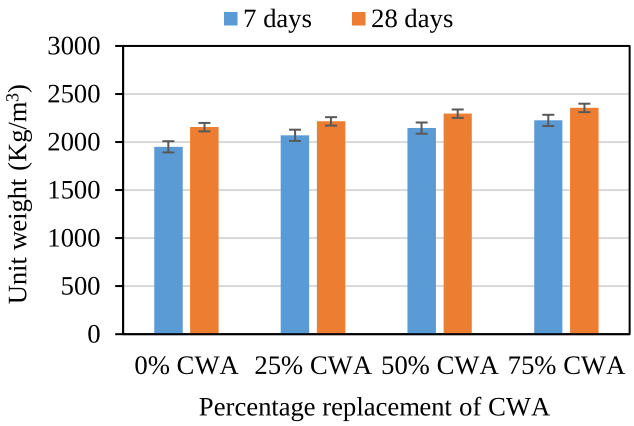

Fig. 5 Comparison of unit weight of brick and CWA concrete

3.3 Mechanical Properties of Concrete Specimens

3.3.1 Compressive Strength

The compressive strength of concrete is significant because it influences the load-bearing capacity and longevity of concrete structures. The compressive strength of the specimen improves with curing periods in both conventional brick aggregate concretes and ceramic waste aggregate concretes, as expected. A different pattern of gaining strength of conventional brick aggregate concrete and CWA concrete can be observed in Fig. 6. At 7 days of curing, the optimum compressive strength of CWA concrete at 50% replacement is 28.95 MPa, which is 15.62% higher than conventional brick aggregate concrete. At 28 days of curing, the maximum compressive strength of CWA concrete at 50% replacement is 31.78 MPa, which is 16.71% higher than conventional concrete. After that 75% replacement, the compressive strength decreases due to the weakness in the concrete mixture, when a high proportion of CWT is used.

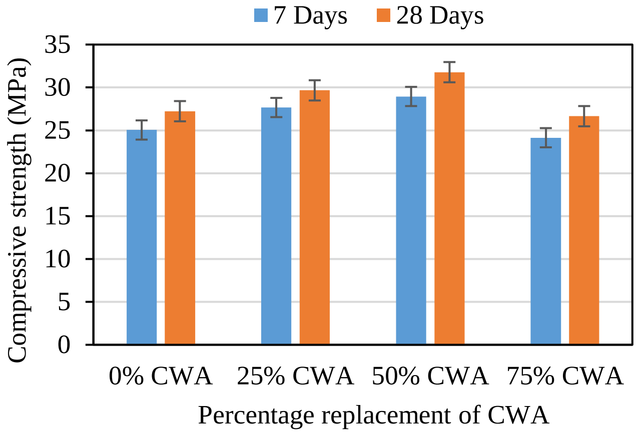

Fig. 6 Comparison of 7 and 28-day compressive strength of brick and CWA concrete

3.3.2 Modulus of Elasticity

The elastic modulus of cylindrical concrete specimens, commonly known as Young's modulus, measures the stiffness or resistance to deformation of the concrete. The modulus of elasticity improved a significant amount by using ceramic waste aggregate in concrete. Fig. 7 shows the variation of the modulus of elasticity at different percentages of replacement of CWA. The modulus of elasticity of concrete for 28 days is more than the 7 days. The optimum modulus of elasticity is obtained at 50% replacement which is 8.07% higher than conventional brick aggregate concrete at 28 days of curing. The modulus of elasticity decreases at 75% replacement due to the differences in properties between CWT and traditional brick chips.

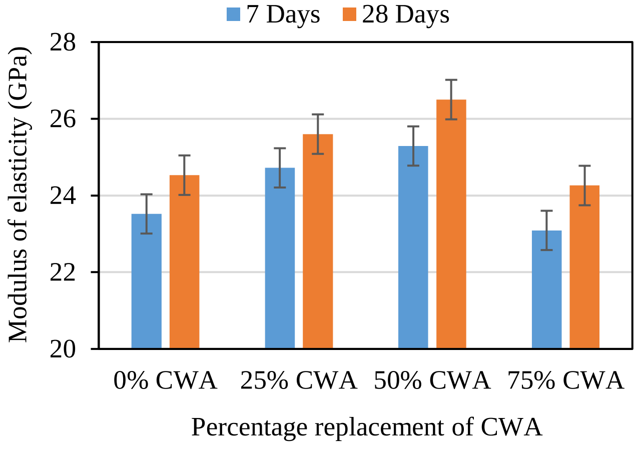

Fig. 7 Modulus of elasticity of brick and CWA concrete at 28 days of curing

3.3.3 Split Tensile Strength

Split tensile strength is a tensile strength measurement of a material, commonly concrete. A compressive load is applied to a cylindrical specimen, causing the cylinder to split along its vertical diameter. In this research, using CWA can significantly improve split tensile strength. Fig. 8 shows the variation of splitting tensile strength after different curing ages. At 50% replacement of CWA, the maximum splitting tensile strength of CWA concrete is 4.04 MPa and 4.45 MPa respectively, at 7 and 28 days of curing, which is 17.78% and 14.10% higher than conventional brick concrete. This improvement is due to the interlocking mechanisms that enhance the overall bonding between the tile and the matrix and decreases after 75% of CWT because of high proportions of CWT.

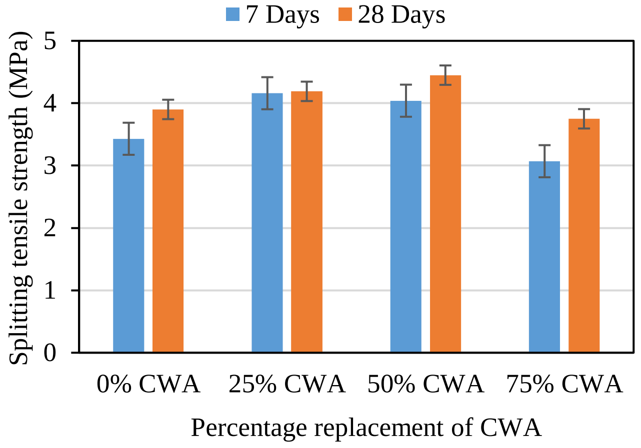

Fig. 8 Comparison of 7 and 28-day split tensile strength of brick and CWA concrete

3.4 Durability Properties of Concrete Specimens

3.4.1 Water Absorption Test

The cylindrical concrete specimen water absorption test is used to assess how much water a concrete sample can absorb. In conventional concrete specimens, the average absorption is 10.70%. But, after the replacement is started, the average absorption decreases by 7.12%, 6.8%, and 6.02%, respectively. Because brick chips have higher water absorption than ceramic tiles waste. If water absorption of the concrete specimen decreases, it indicates that the concrete is less porous and denser. The percentage of water absorption of brick and CWA concrete specimens is shown in Fig. 9.

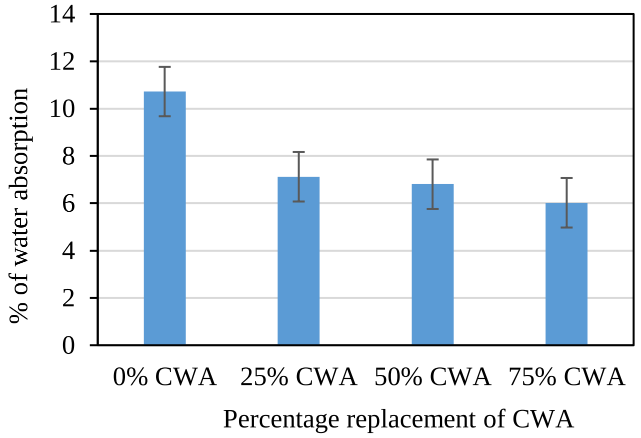

Fig. 9 Comparison average (%) of water absorption of brick to CWA concrete

4 Conclusions

In this research, various percentages of ceramic tile waste (25%, 50%, and 75%) were utilized for producing concrete. The following conclusions were found:

- From the slump value, it can be said that if the amount of CWA is increased, the concrete will be more workable.
- The unit weight of ceramic waste aggregate concrete was high as compared to conventional brick aggregate concrete

specimens due to its higher specific gravity and lower presence of voids.

- For 28 days of curing the maximum compressive strength of CWT concrete is 31.78 MPa which is 16.71% higher than conventional concrete at 50 % substitution.
- The modulus of elasticity is gained at 50% substitution which is 8.07% higher than conventional brick aggregate concrete after 28 days of curing.
- The splitting tensile strength of CWA concrete is almost like the 50% replacement of brick aggregate concrete.
- On the other hand, the water absorption capacity is decreased if the replacement is increased. It indicates that the CWA concrete is less porous and denser.

So, it can be concluded that 50% ceramic waste aggregate substitution in place of brick chips is recommended to produce concrete in terms of mechanical and durability performance.

Acknowledgments

The authors would like to convey their sincere appreciation to the Department of Civil Engineering, HSTU for giving us proper facilities and to the Institute of Research and Training (IRT), HSTU for proper funding for conducting various tests throughout the research works.

References

[1] Goyal, R.K., Agarwal, V., Gupta, R., Rathore, K. and Somani, P., 2022. Optimum utilization of ceramic tile waste for enhancing concrete properties. *Materials Today: Proceedings*, *49*, pp.1769-1775.

[2] Haque, Md Rashedul, Md Shakil Mostafa, and Sujit Kumar Sah. "Performance evaluation for mechanical behaviour of concrete incorporating recycled plastic bottle fibers as locally available materials." *Civil Engineering Journal* 7, no. 4 (2021): 713-719.

[3] Bommisetty, J., Keertan, T.S., Ravitheja, A. and Mahendra, K., 2019. Effect of waste ceramic tiles as a partial replacement of aggregates in concrete. *Materials Today: Proceedings*, *19*, pp.875-877.

[4] Daniyal, M. and Ahmad, S., 2015. Application of waste ceramic tile aggregates in concrete. *International Journal of Innovative Research in Science, Engineering and Technology*, *4*(12), pp.12808-12815.

[5] Halicka, A., Ogrodnik, P. and Zegardlo, B., 2013. Using ceramic sanitary ware waste as concrete aggregate. *Construction and Building Materials*, *48*, pp.295-305.

[6] Prasanna, K. S. A. S. R. K., K. S. Anandh, and S. Ravishankar. "An experimental study on strengthening of concrete mixed with ground granulated blast furnace slag (GGBS)." *ARPN J. Eng. Appl. Sci.* 12, no. 8 (2017): 2439-2444.

[7] Haque, M.R., Hossain, M.B., Roknuzzaman, M., Emu, N.A.A. and Jahan, F.T., 2021. Performance of partially replaced plastic bottles (PET) as coarse aggregate in producing green concrete. *Journal of Brilliant Engineering*, *4*, pp.15-19.

[8] Vijaya, S.K., Jagadeeswari, K. and Srinivas, K., 2021. Behaviour of M60 grade concrete by partial replacement of cement with fly ash, rice husk ash and silica fume. *Materials Today: Proceedings*, *37*, pp.2104-2108.

[9] Pacheco-Torgal, F. and Jalali, S., 2010. Reusing ceramic wastes in concrete. *Construction and building materials*, *24*(5), pp.832-838.

[10] Suzuki, Masahiro, Mohammed Seddik Meddah, and Ryoichi Sato. "Use of porous ceramic waste aggregates for internal curing of high-performance concrete." *Cement and concrete research* 39, no. 5 (2009): 373-381.

[11] Awoyera, P.O., Akinmusuru, J.O. and Ndambuki, J.M., 2016. Green concrete production with ceramic wastes and laterite. *Construction and Building Materials*, *117*, pp.29-36.

[12] Heidari, A. and Tavakoli, D., 2013. A study of the mechanical properties of ground ceramic powder concrete incorporating nano-SiO2 particles. *Construction and building materials*, *38*, pp.255-264.

[13] Devant, M., Cusidó, J.A. and Soriano, C., 2011. Custom formulation of red ceramics with clay, sewage sludge and forest waste. *Applied Clay Science*, *53*(4), pp.669-675.

[14] Mo, K.H., Alengaram, U.J., Jumaat, M.Z., Yap, S.P. and Lee, S.C., 2016. Green concrete partially comprised of farming waste residues: a review. *Journal of Cleaner Production*, *117*, pp.122-138.

[15] Fapohunda, C., Akinbile, B. and Shittu, A., 2017. Structure and properties of mortar and concrete with rice husk ash as partial replacement of ordinary Portland cement–A review. *International Journal of Sustainable Built Environment*, *6*(2), pp.675-692.

[16] Kannan, D.M., Aboubakr, S.H., El-Dieb, A.S. and Taha, M.M.R., 2017. High performance concrete incorporating ceramic waste powder as large partial replacement of Portland cement. *Construction and Building Materials*, *144*, pp.35-41.

[17] Vejmelková, E., Keppert, M., Rovnaníková, P., Ondráček, M., Keršner, Z. and Černý, R., 2012. Properties of high performance concrete containing fine-ground ceramics as supplementary cementitious material. *Cement and Concrete Composites*, *34*(1), pp.55-61.

[18] Elçi, H., 2016. Utilisation of crushed floor and wall tile wastes as aggregate in concrete production. *Journal of Cleaner Production*, *112*, pp.742-752.

[19] Binici, H., 2007. Effect of crushed ceramic and basaltic pumice as fine aggregates on concrete mortars properties. *Construction and building materials*, *21*(6), pp.1191-1197.

[20] Amin, M., Tayeh, B.A. and Agwa, I.S., 2020. Effect of using mineral admixtures and ceramic wastes as coarse aggregates on properties of ultrahigh-performance concrete. *Journal of Cleaner Production*, *273*, p.123073.

[21] Ali, T., Saand, A., Bangwar, D.K., Buller, A.S. and Ahmed, Z., 2021. Mechanical and durability properties of aerated concrete incorporating rice husk ash (RHA) as partial replacement of cement. *Crystals*, *11*(6), p.604.

[22] ASTM C136 / C136M-14, “Standard Test Method for Sieve Analysis of Fine and Coarse Aggregates, ASTM International, West Conshohocken, PA, 2014”.

[23] ASTM C29/C29M-97, “Standard Test Method for Bulk Density (“Unit Weight”) and Voids in Aggregate, ASTM International, West Conshohocken, PA, 1997”.

[24] ASTM C127-15, Standard Test Method for Relative Density (“Specific Gravity”) and Absorption of Coarse Aggregate, ASTM International, West Conshohocken, PA, 1997.”

[25] ASTM C128-15, Standard Test Method for Relative Density (“Specific Gravity”) and Absorption of Fine Aggregate, ASTM International, West Conshohocken, PA, 1997.”

[26] ASTM C143/C143M-15, “Standard Test Method for Slump of Hydraulic-Cement Concrete”.

[27] ASTM C39/C39M-18, “Standard Test Method for Compressive Strength of Cylindrical Concrete Specimens”.

[28] ASTM C496/C496M-17, “Standard Test Method for Splitting Tensile Strength of Cylindrical Concrete Specimens”.

SciEn
Journal of Engineering Advancements Vol. 05(01) 2024, pp 14-18 https://doi.org/10.38032/jea.2024.01.003

Heat Transfer Mechanism over a Trapezium-Shaped Device Including Heat Conductive Solid Circular Metal Block

M. U. Ahammad, Abdur Rahim, Abu Hanifa

Department of Mathematics, Dhaka University of Engineering and Technology, Gazipur-1707, Bangladesh

Received: November 26, 2023, Revised: February 08, 2024, Accepted: February 08, 2024, Available Online: March 10, 2024

ABSTRACT

Combined convective flow design and heat transfer efficiency are investigated in this research for variation of some pertinent parameters inside a trapezoidal device along with heat conductive solid circular block. By the implementation of the Finite element method, flow, and heat transfer behavior are presented in detail for the ranges of Reynolds number, $50 \leq \mathrm{Re} \leq 200$, and Hartmann number, $20 \leq \mathrm{Ha} \leq 150$ along with mixed convection parameter Ri = 1. Obtained results for the flow and temperature field in the considered domain are shown in terms of the streamlines and isotherms. In addition, the heat transfer rate at the bottom heated and ceiling cold wall is presented by $Nu_{av.}$ A noteworthy heat transfer augmentation is found at both heated and cold surfaces due to upper values of Re. Interestingly, the better cooling efficiency of the device is marked out for the hot wall.

Keywords: Heat Transfer, Trapezoidal Device, Heat Conduction, Solid Metal Block.

1 Introduction

Free and forced convection is a crucial issue in fluid flow and thermal systems of different geometrical configurations. Due to the many engineering and industrial applications, such types of phenomena have received great concentration from researchers and are frequently encountered in cooling systems for electronic equipment, thermal insulation, energy storage, and heat exchangers.

Mamun *et al.* [1] analyzed mixed convection analysis in the trapezoidal cavity with a moving lid. Two-dimensional MHD free convection with internal heating in a square cavity was presented by Taghikhani and Chavoshi [2]. Mixed convection enhancement in a rectangular cavity by triangular obstacle was presented by Afluq *et al.* [3]. Ibrahim and Hirpho [4] carried out combined convection flow in a trapezoidal domain taking non-uniform temperature. Abdul Halim Bhuiyan *et al.* [5] studied the effect of the Hartmann Number on free convective flow in a square cavity with different positions of heated square block. Shuja *et al.* [6] performed a heat-generating rectangular body effect of cavity exit port locations in a square enclosure. Mixed convection from an isolated heat source in a rectangular enclosure was performed by Papanicolaou and Jaluria [7]. Raji and Hasnaoui *et al.* [8] presented mixed convection heat transfer in a rectangular cavity ventilated and heated from the side. An experimental investigation of combined convection in a channel with a vented cavity was carried out by Manca *et al.* [9]. Analysis of free convection around a square heated cylinder kept in a cavity was explained by Kumar and Dalal [10]. Rahman *et al.* [11] performed mixed convection in a vented square cavity with a heat-conducting horizontal solid circular cylinder. Gau *et al.* [12] investigated an experimental study on mixed convection in a horizontal rectangular channel heated from a side. Sheremet *et al.* [13] studied natural convective heat transfer through two entrapped triangular cavities filled with a nanofluid. Brown *et al.* [14] studied mixed convection from an open cavity in a horizontal channel.

From the literature cited above and according to the authors' knowledge, it is followed that no work has been performed yet for the specified configuration of the current problem. The goal of the present research is to investigate combined convection flow and heat transfer behavior in a trapezoidal-shaped domain having a heat conductive circular block for the variation of Reynolds and Hartmann number.

2 Geometry and Mathematical Model

The considered domain of this problem is depicted in Fig. 1, which is formed by a trapezoidal enclosure whose lower and upper sides are of the length $2L$ and $L/2$ respectively. A heat-conductive circular block is placed at the center of the cavity. The bottom surface is heated and the top surface is cooled accordingly as $T_h > T_c$. The two inclined walls of the domain are considered adiabatic. A uniform magnetic field of strength B_0 is applied to the flat direction of the left wall.

In the current study, the working fluid is considered as 2-D steady, laminar, and Newtonian with constant thermo-physical properties. The leading equations for the problem in non-dimensional form are given below:

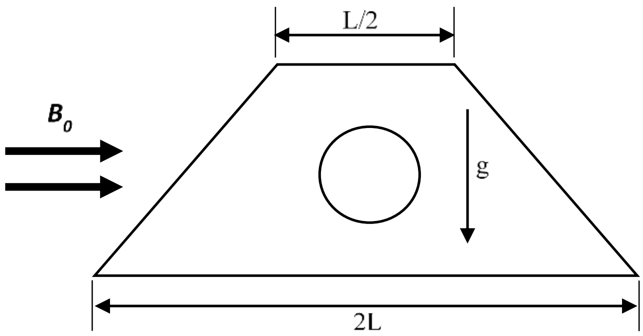

Fig. 1 Schematic sketch of the problem

*Corresponding Author Email Address: mainuddin633@duet.ac.bd Published by: SciEn Publishing Group

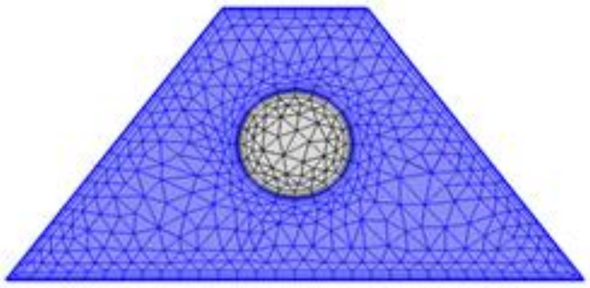

Fig. 2 Typical Grid generation

$$\frac{\partial U}{\partial X}+\frac{\partial V}{\partial Y}=0 \tag{1}$$

$$U\frac{\partial U}{\partial X}+V\frac{\partial U}{\partial Y}=-\frac{\partial P}{\partial X}+\frac{1}{Re}\left(\frac{\partial^2 U}{\partial X^2}+\frac{\partial^2 U}{\partial Y^2}\right) \tag{2}$$

$$U\frac{\partial V}{\partial X}+V\frac{\partial V}{\partial Y}=-\frac{\partial P}{\partial X}+\frac{1}{Re}\left(\frac{\partial^2 V}{\partial X^2}+\frac{\partial^2 V}{\partial Y^2}\right)+Ri\theta-\frac{Ha^2}{Re}V \tag{3}$$

$$U\frac{\partial \theta}{\partial X}+V\frac{\partial \theta}{\partial Y}=\frac{1}{RePr}\left(\frac{\partial^2 \theta}{\partial X^2}+\frac{\partial^2 \theta}{\partial Y^2}\right) \tag{4}$$

For heat-conducting circular body,

$$\frac{K}{RePr}\left(\frac{\partial^2 \theta_s}{\partial X^2}+\frac{\partial^2 \theta_s}{\partial Y^2}\right) \tag{5}$$

The following non-dimensional variables are used in order to obtain the above dimensionless governing Eqs. (1)−(5), $X=\frac{x}{L},\ Y=\frac{Y}{L},\ U=\frac{u}{u_i}, V=\frac{v}{u_i}, P=\frac{p}{\rho u_i^2},\ \theta=\frac{(T-T_C)}{(T_h-T_C)},\ \theta_s=\frac{(T_s-T_c)}{(T_h-T_c)}$

Where X and Y are the coordinates varying along horizontal and vertical directions; U, and V are the velocity components in the X and Y directions respectively. Also θ and θ_s are the dimensionless temperature of fluid and solid respectively and P is the dimensionless pressure.

The governing parameters are defined correspondingly as

$$Re=\frac{u_i L}{v},\ Pr=\frac{v}{\alpha},\ Ha=B_0 L\sqrt{\frac{\sigma}{\mu}},\ Ri=\frac{Gr}{Re^2}$$

($u_i$is the reference velocity of fluid and B0 is magnetic field strength)

The imposed boundary conditions are as follows:

At upper surface: $U=0, V=0, \theta=0$; at lower surface: $U=0, V=0, \theta=1$; and at two side walls: $U=0, V=0, \frac{\partial\theta}{\partial N}=0$

Also, Nu_{av} at the heated wall is calculated using $Nu_{av}=-\int_0^1\left(\frac{\partial\theta}{\partial Y}\right)dX$

3 Grid Refinement Test and Validity of the Code

Various grid-sized elements are taken to find the optimum accurateness of the result for the considered problem. A typical grid size distribution is shown in Fig. 2. The heat transfer rate at the bottom wall of the cavity is calculated for the selected grids. A slight difference is noticed among the results for the variation of grid size which is tabulated in Table 1. Finally, the grid containing 2184 elements is taken into account for computing Nu_{av} at the hot wall. Table 2 shows the thermo-physical properties of water and aluminum used in this work.

Table 1 Nu_{av} at bottom surface for Pr = 7.1, Re = 100, Ha = 20, Ri = 1

No. of elements	621	886	1456	2184	3384
Nu_{av}	6.9638	6.9062	6.8694	6.8677	6.8662
Deviation	-	0.0576	0.0368	0.0017	0.0015

Table 2 Thermo physical properties of water and aluminum

Property	Water	Aluminum (Al)
$C_p\ (Jkg^{-1}K^{-1})$	4179	902
$\rho\ (kgm^{-3})$	997.1	2701
$k\ (Wm^{-1}K^{-1})$	0.613	237
$\beta\ (K^{-1})$	21×10^{-5}	23.1×10^{-6}
$\sigma\ (S/m)$	.05	3.5×10^{7}

For the code validation of the present work, a computation is performed for comparison with the previously published work that was performed by the authors Ibrahim and Hirpho [4]. Fig. 3 exposes the relationship between these two works with a good agreement in velocity and temperature fields that are demonstrated as streamlines and isotherms.

4 Results and Discussions

In this work, two-dimensional steady flow and thermal field are investigated to test the effect of Re and Ha inside the studied configuration. The streamlines, isotherms, and average Nusselt number are exhibited to clarify the flow and temperature ground of the problem for the range of Hartmann number 20 ≤ Ha ≤ 150 along with mixed convection parameter Ri = 1 and Prandtl number Pr = 7.1.

Reynolds number's effect on velocity and temperature profile in the range of 50 to 200 is displayed in Fig. 4. Fig. 4 (a) exposes that at low Reynolds number Re = 50, large-sized vortexes are created surrounding the centered circular block. For the next higher values Re = 100 and Re = 150, the flow patterns are all most similar. But for the largest value of Re = 200, the intensity of the left-sided vortex increases consequently vorticity of the right-sided vortex reduces.

In Fig. 4 (b), the isotherms for different Reynolds numbers are exposed and this figure shows that heat lines are non-linear occupying the total region and dense in the neighborhood of the top cooled wall at Re = 50. Also, the centered body is encircled by the thermal lines and comparatively more heated lines are found near the heated lower surface. No visible alteration is tracked for the three rising values of Re = 100, 150, 200.

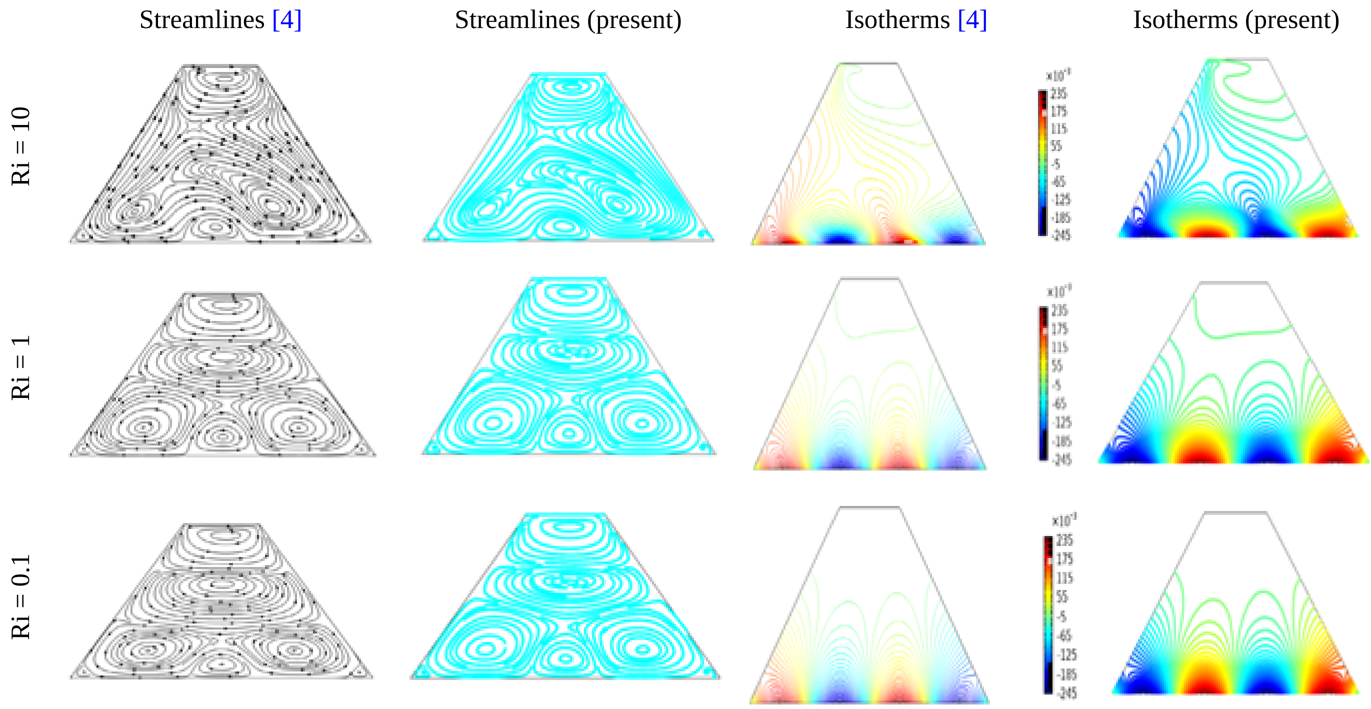

(a) Streamlines (b) Isotherms

Fig. 3 Relationship between the present and the work of Ibrahim and Hirpho [4] at Gr = 10^4, Pr = 6.2, Ha = 50, and Re = 100

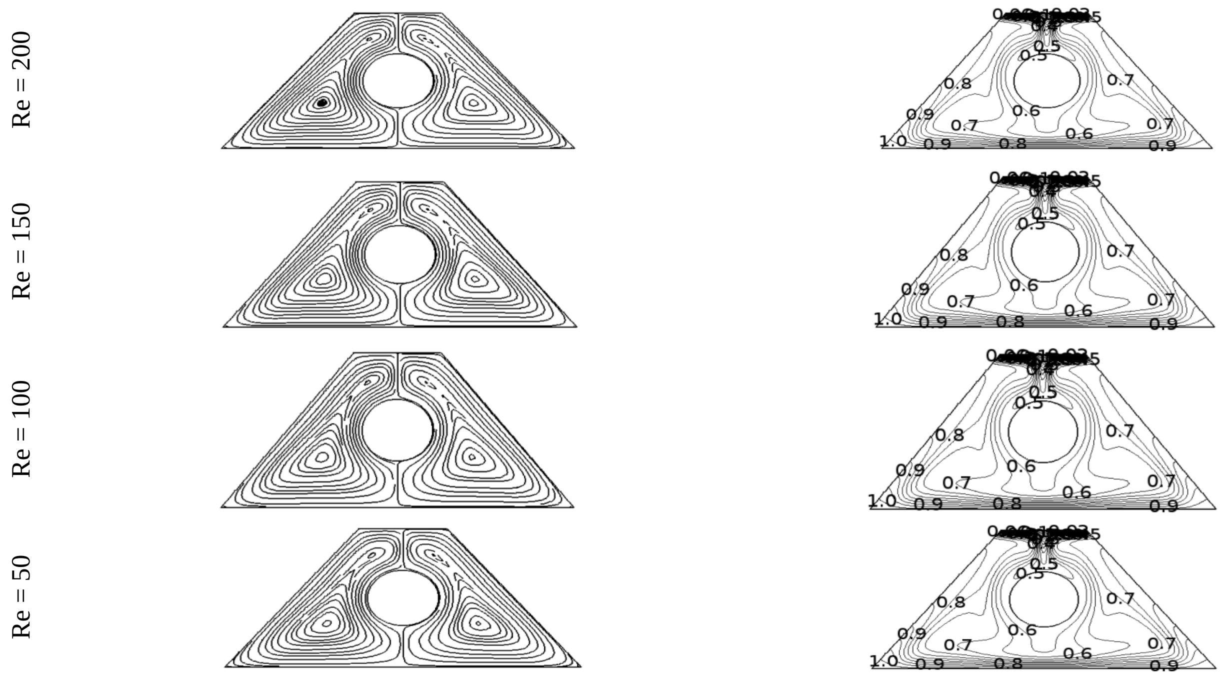

(a) (b

Fig. 4 (a) Streamlines and (b) Isotherms for variation of Re at Pr =7.1, Ri = 1, Ha = 20

In Fig. 5, streamlines and isotherms are exhibited for the various values of Ha that vary from 20 to 150. One can observe from Fig. 5(a) that at low Hartmann number Ha = 20 the streamlines captured the whole cavity by the about two symmetric vortices concerning the interior body. A minor discrepancy is noticed for Ha = 50. For the mounting values of Ha = 100 and Ha = 150 a significant change is noticed, the vortex strength increases near the bottom and top surface, especially for Ha = 150.

The corresponding thermal lines distributions in the enclosure for different Hartmann numbers are illustrated in Fig. 5 (b). With a small change the heat lines are found non-uniform that are elongated from the left side to the right side of the cavity for Ha = 20 and Ha = 50. A thick boundary layer is created at the top wall. In addition, heat lines are comparatively linear and symmetric about the circular body for the two larger values of Ha = 100 and Ha = 150. More heated heat lines are located at the bottom part of the enclosure; thermal lines are concentrated above the circular block.

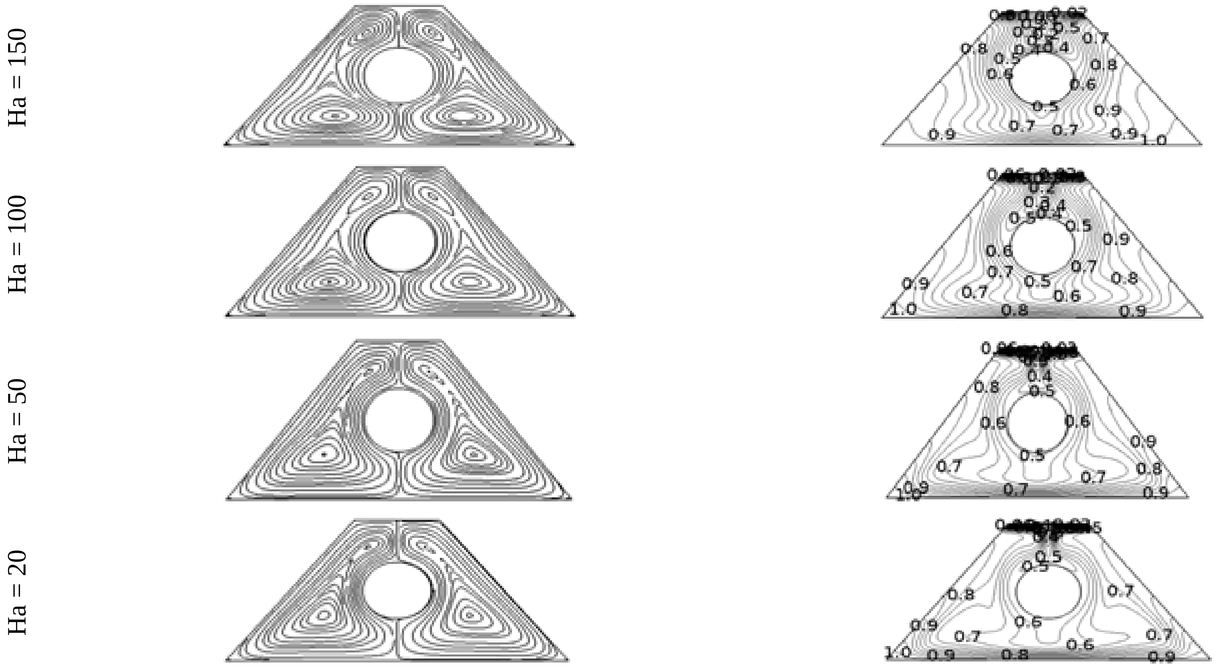

(a) (b)

Fig. 5 (a) Streamlines and (b) Isotherms for different values of Ha at Pr =7.1, Ri = 1, Re =100

Fig. 6 shows the average Nusselt number at both heated and cold wall for the variation of (a) Reynolds number and (b) Hartmann number. This figure reveals that higher heat removal is obtained for the upper values of Reynolds number while Nu_{av} reduces for the higher values of Ha due to its resistance.

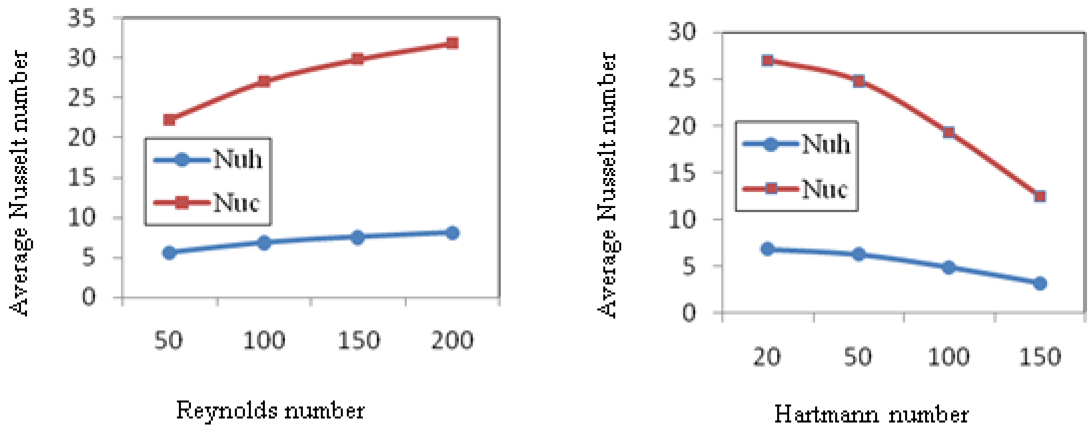

Fig. 6 Heat transfer rate at ceiling and ground walls for different values of (a) Reynolds number and (b) Hartmann number

The rate of heat transfer at bottom heated and top cooled walls for chosen values of Reynolds number are shown in Table 3. From the table, it can be followed that the heat removal rate at hot and cool walls increases with the mounting values of Re and vice versa.

Table 3 Average Nusselt number for variation of Re while Pr = 7.1, Ha = 20 and Ri = 1

Re	$(Nu_{av})_{hot}$	$(Nu_{av})_{cool}$
50	5.6635	22.206
100	6.8677	26.980
150	7.5679	29.765
200	8.0859	31.806

Nu_{av} at ground and ceiling surfaces for different values of Ha that are listed in Table 4 and it is noticed that cooling efficiency at both walls enhances the smaller values of Ha.

Table 4 Average Nusselt number for variation of Ha while Pr = 7.1, Re = 100 and Ri = 1

Ha	$(Nu_{av})_{hot}$	$(Nu_{av})_{R\ cool}$
20	6.8677	26.980
50	6.3227	24.804
100	4.9307	19.279
150	3.2079	12.496

5 Conclusions

The influence of Re and Ha along with Ri on flow and thermal field have been analyzed in a trapezoidal domain with an internal heat conductive circular body. The obtained results of the problem are stated concisely below:

- Significant improvement in heat transfer is recorded at both hot and cold walls due to higher values of Re, consequently smaller value of Reynolds number gives the lowest heat removal.
- As Ha increases, Nu_{av} decreases at the heated and cold surface, so optimum heat transfer is found for the lowest Hartmann number.
- Comparatively rapid change in heat removal is followed at the bottom heated wall.

References

[1] Mamun, M.A.H., Tanim, T.R., Rahman, M.M., Saidur, R. and Nagata, S., 2010. Mixed convection analysis in trapezoidal cavity with a moving lid. International Journal of Mechanical and Materials Engineering, 5(1), pp.18-28.

[2] Taghikhani, M.A. and Chavoshi, H.R., 2013. Two dimensional MHD free convection with internal heating in a square cavity. Thermal Energy and Power Engineering, 2(1), pp.22-28.

[3] Afluq, S.G., Siba, M.A.A.A. and Jehhef, K.A., 2020, July. Mixed convection enhancement in a rectangular cavity by triangular obstacle. In IOP Conference Series: Materials Science and Engineering (Vol. 881, No. 1, p. 012083). IOP Publishing.

[4] Ibrahim, W. and Hirpho, M., 2021. Finite element analysis of mixed convection flow in a trapezoidal cavity with non-uniform temperature. Heliyon, 7(1).

[5] Bhuiyan, A.H., Alim, M.A. and Uddin, M.N., 2014. Effect of Hartmann number on free convective flow in a square cavity with different positions of heated square block. International Journal of Physical and Mathematical Sciences, 8(2), pp.385-390.

[6] Obayedullah, M., Chowdhury, M.M.K. and Rahman, M.M., 2013. Natural convection in a rectangular cavity having internal energy sources and electrically conducting fluid with sinusoidal temperature at the bottom wall. International Journal of Mechanical and Materials Engineering, 8(1), pp.73-78.

[7] Papanicolaou, E. and Jaluria, Y., 1991. Mixed convection from an isolated heat source in a rectangular enclosure. Numerical Heat Transfer, 18(4), pp.427-461.

[8] Raji, A. and Hasnaoui, M., 1998. Mixed convection heat transfer in a rectangular cavity ventilated and heated from the side. Numerical Heat Transfer, Part A Applications, 33(5), pp.533-548.

[9] Manca, O., Nardini, S. and Vafai, K., 2006. Experimental investigation of mixed convection in a channel with an open cavity. Experimental heat transfer, 19(1), pp.53-68.

[10] De, A.K. and Dalal, A., 2006. A numerical study of natural convection around a square, horizontal, heated cylinder placed in an enclosure. International journal of heat and mass transfer, 49(23-24), pp.4608-4623.

[11] Rahman, M., Alim, M.A., Saha, S. and Chowdhury, M.K., 2008. Mixed convection in a vented square cavity with a heat conducting horizontal solid circular cylinder. Journal of naval architecture and marine engineering, 5(2), pp.37-46.

[12] Gau, C., Jeng, Y.C. and Liu, C.G., 2000. An experimental study on mixed convection in a horizontal rectangular channel heated from a side. J. Heat Transfer, 122(4), pp.701-707.

[13] Sheremet, M.A., Revnic, C. and Pop, I., 2017. Natural convective heat transfer through two entrapped triangular cavities filled with a nanofluid: Buongiorno's mathematical model. International journal of mechanical sciences, 133, pp.484-494.

[14] Leong, J.C., Brown, N.M. and Lai, F.C., 2005. Mixed convection from an open cavity in a horizontal channel. International Communications in Heat and Mass Transfer, 32(5), pp.583-592.

SciEn
Journal of Engineering Advancements Vol. 05(01) 2024, pp 19-26 https://doi.org/10.38032/jea.2024.01.004

Improvement of the Nearest Neighbor Heuristic Search Algorithm for Traveling Salesman Problem

Md. Ziaur Rahman[1], Sakibur Rahamn Sheikh[2], Ariful Islam[2], and Md. Azizur Rahman[2,]*

[1]Department of Mathematics, Bangladesh University of Engineering and Technology (BUET), Dhaka-1000, Bangladesh
[2]Mathematics Discipline, Khulna University, Khulna-9208, Bangladesh

Received: December 21, 2023, Revised: February 27, 2024, Accepted: March 01, 2024, Available Online: March 30, 2024

ABSTRACT

The Traveling Salesman Problem (TSP) is classified as a non-deterministic polynomial (NP) hard problem, which has found widespread application in several scientific and technological domains. Due to its NP-hard nature, it is very hard to solve effectively and efficiently. Despite this rationale, a multitude of optimization approaches have been proposed and developed by scientists and researchers during the last several decades. Among these several algorithms, heuristic approaches are deemed appropriate for addressing this intricate issue. One of the simplest and most easily implementable heuristic algorithms for TSP is the nearest neighbor algorithm (NNA). However, its solution quality suffers owing to randomness in the optimization process. To address this issue, this study proposes a deterministic NNA for solving symmetric TSP. It is an improved version of NNA, which starts with the shortest edge consisting of two cities and then repeatedly includes the closest city on the route until an effective route is established. The simulation is conducted on 20 benchmark symmetric TSP datasets obtained from TSPLIB. The simulation results provide evidence that the improved NNA outperforms the basic NNA throughout most of the datasets in terms of solution quality as well as computational time.

Keywords: Combinatorial Optimization, Traveling Salesman Problem (TSP), Heuristic Algorithm, Nearest Neighbor Algorithm, Improved Nearest Neighbor Algorithm

1 Introduction

Combinatorial optimization problems are of interest to several academic disciplines, including theoretical computer science, artificial intelligence, operations research, and discrete mathematics. One of the most prominent combinatorial optimization problems is the traveling salesman problem (TSP), which is studied in several disciplines including mathematics, artificial intelligence, physics, operations research, and biology. The task at hand pertains to the identification of the most efficient route connecting a collection of cities, with the constraint that each city be visited only once before returning to the initial city [1]. The origins of the Traveling Salesman Problem are believed to have been uncovered in Vienna in 1920 [2]. In 1954, Dantzig *et al.* [3] provided a formal elucidation of the traveling salesman problem. Subsequently, this methodology has been extensively employed to simulate and analyze various practical scenarios, encompassing domains such as hardware design, microchip design, radio-electronic device design, data association, data transmission in computer networks, DNA sequencing, vehicle routing, job scheduling, clustering of data arrays, image processing and pattern recognition, crystal structure analysis, transportation, logistics, and supply chain management [4]-[5]. The TSP is characterized by its comprehensibility, although it often poses challenges when attempting to find a solution due to its inclusion of all relevant components inside a combinatorial optimization framework. Undoubtedly, the computational time required to solve the TSP increases exponentially as the number of cities increases, as shown by Hore *et al.* [5]. Hence, the investigation into enhancing the solution method for the TSP has significant theoretical, technical, and practical implications.

In graph theory, the TSP can be defined symmetrically on a full undirected graph $G = (V, E)$ or asymmetrically on a directed graph $G = (V, A)$, where $V = \{1,2,3,\ldots n\}$ is the set of vertices, $E = \{(i,j): i,j \in V, i < j\}$ is a set of edge and $A = \{(i,j): i,j \in V, i \neq j\}\}$ is a set of arcs. On E or on A a cost matrix $C = (c_{ij})$ is defined. Each edge is assigned a cost, which is the distance between cities i and j, can be defined as [6]:

$$c_{ij} = \sqrt{(x_i - x_j)^2 + (y_i - y_j)^2}$$

Depending on the distance matrix C, the TSP can be categorized as symmetric or asymmetric. G is symmetric TSP if $c_{ij} = c_{ji}$ and asymmetric TSP if $c_{ij} \neq c_{ji}$. In this paper we use symmetric TSP (sTSP). The objective function Z written as [6]:

$$Z = Min \sum_{i,j \in V, i<j} c_{ij} x_{ij} \tag{1}$$

and decision variable

$$x_{ij} = \begin{cases} 1 \ ; \textit{the routes connects cities i and j} \\ 0 \ ; \textit{otherwise} \end{cases} \tag{2}$$

with respect to the following constrains [6]:

$$\sum_{i,j \in V} x_{ij} = n \tag{3}$$

$$\sum_{i<k} x_{ik} + \sum_{k<j} x_{kj} = 2 \tag{4}$$

$$\sum_{i<j} x_{ij} \leq |T| - 1 \ (T \subset V, 2 \leq |T| \leq n-2) \tag{5}$$

*Corresponding Author Email Address: mdazizur@math.ku.ac.bd
Published by: SciEn Publishing Group

Here, Eq. (1) represents the objective function, which aims to minimize the overall distance, Eq. (2) denotes the decision variable, while Eqs. (3) - (5) provide the constraints that must be satisfied in the model. a binary variable x_{ij} is associated with each edge (i, j) in the graph G, as shown by Eq. (2). The values 1 and 0 of x_{ij} indicate whether each edge (i, j) should be included or excluded from the optimum route. As seen in the Eq. (3) above, it is evident that every possible path, including the optimal path, must consist of exactly n edges. According to Eq. (4), it is necessary to choose exactly two edges for every vertex. This constraint facilitates the establishment of itineraries in which each city is visited just once, with the salesman ultimately returning to the initial location. Eq. (5) serves as a constraint that prohibits the creation of sub routes with fewer vertices than the total number of vertices, denoted as n. This requirement ensures that all cities are visited [6].

Due of its applicability and complexity, several scholars have conceived and developed different optimization techniques in the past few decades to cope with the TSP issue. Heuristic algorithms are the most successful and frequently utilized search approach for tackling the TSP issue among these algorithms [1]. One of the simplest and most easily implementable heuristic algorithms for TSP is the Nearest Neighbor Algorithm (NNA). However, its solution quality suffers from the randomness inherent in the optimization process. In this paper, we improve the basic NNA for symmetric TSP. Indeed, the improved version of NNA is a deterministic approach that begins with an edge of the two closest cities and connects them simultaneously with the next-closest cities one by one until feasible routes are formed. The proposed improved version shows better performance than the basic NNA in terms of solution quality as well as simulation time. The present paper is organized as follows. Some engineering applications of the TSP are presented in Section 2. In Section 3, we review some related works to solve symmetric problem. The methods of study including both improved and basic NNA are presented in detail in Section 4. In Section 5, the results are given and discussed, and Section 6 concludes the study with a future plan.

2 Some Engineering Applications of TSP

The traveling salesman problem (TSP) is an extensively studied problem in computer science and optimization theory, but it also has numerous real-life applications in diverse engineering fields. Here are some engineering applications of TSP:

Circuit Board Manufacturing: In electronics manufacturing, the TSP can be used to optimize component placement on circuit boards. By finding the shortest path that visits all the required connection points (components), engineers can minimize the length of interconnect lengths, reduce signal delays, and optimize the layout for space and efficiency.

Robotics: TSP algorithms are used in robotics for motion planning, task allocation, and multi-robot coordination. These algorithms help discover a shortest path for a robot to traverse multiple points in a given environment while satisfying constraints such as avoiding obstacles and obeying motion limits (e.g., maximum speed, acceleration). This is crucial for tasks such as robotic exploration, surveillance, and delivery in known or unknown terrain environments.

DNA Sequencing: In bioinformatics, the TSP has been adopted to solve DNA sequencing problems, where the goal is to determine the most efficient order in which to sequence fragments of DNA to reconstruct the original sequence. By leveraging TSP algorithms, researchers can enhance the efficiency, accuracy, and scalability of DNA sequencing workflows and data analysis pipelines.

Wireless Sensor Networks (WSNs): TSP algorithms provide powerful optimization tools to address various challenges in WSNs, including data collection, energy efficiency, coverage optimization, fault detection, and dynamic network management. With the TSP algorithms, researchers and engineers can design more efficient and robust WSNs for a wide range of applications, including environmental monitoring, smart infrastructure, and IoT systems.

Vehicle Routing and Logistics: One of the most common applications of TSP is optimizing routes for delivery vehicles, such as trucks, drones, or even autonomous vehicles. By finding the shortest route that visits a set of locations (cities or delivery points), companies can minimize fuel consumption, reduce travel time, and improve overall efficiency in logistics operations while meeting various operational constraints.

Urban Planning: In urban planning, TSP algorithms can assist in optimizing routes for garbage collection trucks, street cleaning vehicles, and other municipal services, leading to more efficient use of resources and reduced traffic congestion.

VLSI Chip Design: In VLSI (Very Large Scale Integration) chip design, TSP algorithms are utilized for tasks such as wire routing and layout optimization. By finding the shortest paths to connect different components on the chip, engineers can reduce cable length, reduce signal delay, and optimize chip area and power consumption.

These are just a few examples, and the applications of the TSP in engineering are diverse and continually evolving as new challenges arise in various fields.

3 Related Works

Nearest Neighbor Algorithm (NNA) is one of the simplest heuristic route construction algorithms. For a long time, researchers have been working on this route construction algorithm for solving TSP. In this section, we review some works that researchers have done recently on the route construction algorithm for TSP.

Hore *et al*. [5] offered a greedy algorithm-based solution to the traveling salesman issue. The greedy algorithm is like the Nearest Neighbor Algorithm (NNA), and the route starts from that particular sub-route with two cities, which has the shortest distance among all such feasible sub-routes. Although such an algorithm usually does not give the global optimum solution, it has been considered the initial solution. These algorithms are compared to their proposed algorithm. The suggested approach outperformed the conventional approaches and was determined to be more effective than the VNS-1 and VNS-2 algorithms on average. In their paper, Naser *et al.* [7] introduced a deterministic methodology that used a multi-perfect matching and partitioning technique to approximate the solution of the symmetric traveling salesman problem (STSP). The first step was identifying the most cost-effective combination of sub-routes that encompassed all cities and had a minimum of four edges for each sub-route. The performance of the proposed method is assessed and contrasted with the optimum values achieved by other established strategies for solving the Symmetric Traveling Salesman Problem (STSP). The simulation results presented in this paper indicate that the methodology used by the researchers yields solutions that are either optimum or very close to optimal within a polynomial time frame.

Halim and Ismail [8] conducted a comparative analysis of heuristic strategies in the Traveling Salesman Problem (TSP). The study focused on six heuristic approaches, namely Nearest Neighbor, Genetic Algorithm, Simulated Annealing, Tabu Search, Ant Colony Optimization, and Tree Physiology Optimization. The comparison of computation, accuracy, and convergence has been conducted in this research. Bentley [9] employed a double-sided NN method, which allows the route to improve on both ends. This method uses nearest neighbour (NN) search on both ends of the route to find the path with the shortest length. On the other hand, Klug *et al.* [10] have recently expanded the NN technique to k-RNN for solving STSP and ATSP. The simulation results indicated that the solution quality of the 2-RNN algorithm remains rather consistent, ranging from around 10% to 40% higher than the optimal solution.

Bakar and Ibrahim [11] used a heuristic shortest route methodology in order to determine the optimal solution for the TSP. This study proposes a modified strategy that combines the heuristic shortest distance method and fuzzy approach for addressing a network with an erroneous arc length. The investigation focused on the determination of the network's arc length, as well as the analysis of the interval number and triangular fuzzy number. Subsequently, the revised methodology was used to address a particular instance of the Traveling Salesman Problem (TSP). The overall shortest distance obtained using this strategy was then compared to the total distance generated by employing a conventional nearest neighbor heuristic technique. The findings indicate that the modified methodology yields a sequence of visited cities that is equivalent to the conventional technique. Additionally, it provides a reliable measure of the total shortest distance, which is less than the total shortest distance calculated by the old approach. Consequently, the findings of this study have the potential to enhance the existing methodologies used in addressing the TSP.

The heuristic approach proposed by Lin *et al.* [12] for the TSP is highly commendable. The authors introduced a heuristic approach that demonstrated significant success in generating optimal and near-optimal solutions for the STSP. The methodology was formulated employing a comprehensive heuristic approach that possesses the potential to address diverse combinatorial optimization problems. The proposed methodology successfully produced optimal solutions for all the examined problems, encompassing both "traditional" problems documented in existing literature and randomly generated problems. The scope of the problems ranged up to a maximum of 110 cities. In terms of absolute values, it was observed that a typical issue involving 100 cities required less than 25 seconds for a single example (GE635) and approximately three minutes to reach the optimal solution with a confidence level exceeding 95%. In addition, some papers are reviewed on the Nearest Neighbor Algorithm (NNA) for TSP are mentioned in [13]-[17].

4 Methods of Study

4.1 Basic Nearest Neighbor Algorithm

The most elementary algorithm employed in the Traveling Salesman Problem (TSP) is the Nearest Neighbor Algorithm (NNA). The aforementioned approach efficiently produces a concise route, albeit infrequently yielding the optimal solution [18]. The basic NNA is used to determine a traveling salesman's itinerary. The salesperson begins in one city (at random), then travels to the city closest to the beginning city. After that, he travels to the nearest unexplored city and continues the procedure until all of the cities have been visited, at which point he returns to the beginning city. The basic NNA algorithm is as follows:

1. Make all vertices unvisited by default
2. Select a random vertex and make it the current vertex $\boldsymbol{u}$. Make a note that $\boldsymbol{u}$ has been visited
3. Find the shortest path between current vertex $\boldsymbol{u}$ and a previously visited vertex $\boldsymbol{v}$
4. Set the current vertex $\boldsymbol{u}$ to $\boldsymbol{v}$. Make a note that $\boldsymbol{v}$ has been visited
5. Terminate when all of the domain's vertices have been visited. Otherwise, proceed to step 3
6. Return to your starting city

However, its solution quality suffers owing to randomness. Due to the problem, we have proposed a revised version of the basic NNA. The basic NNA is mostly probabilistic because it cannot always provide the shortest route. But the improved algorithm is deterministic. The improved NNA is a route-construction algorithm. First, it chooses a random city from a list of cities in NNA. Then, using the shortest distance, travel to the nearest unexplored city. This process will be repeated until all cities have been visited and the player is forced to return to the starting point.

4.2 Improved Nearest Neighbor Algorithm

It began its route on the improved NNA with a short distance. Firstly, it sorts all edges, and then it takes a short edge with two vertices (or cities). This is the main difference between improved NNA and basic NNA. The next steps of the improved NNA are like those of the basic NNA. The mathematical analysis and algorithm of an improved NNA are discussed in the following subsection.

Let n be the number of cities and TSP can be defined symmetrically on a full undirected graph $G=(V,E)$, where $V=\{A_1,A_2,A_3,\ldots,A_n\}$ is the set of vertices, $E=\{(A_i,A_j): A_i,A_j\in V, i>j\}$ is a set of edge. Then, calculate the distance of every possible edge and select the shortest edge contains two closest cites A_i and A_j which is our initial edge and expressed as $A_i\leftrightarrow A_j$.

The set of routes is,

$$X_1=min\{A_iA_j: i=1,2,\ldots,n \text{ and } j=1,2,\ldots,n-1 \text{ and } A_iA_j\in E\}$$

Now, choose the nearest city A_k from the initial edge and connect the city which is expressed as

$$A_i\leftrightarrow A_j\leftrightarrow A_k$$

and the set of the route is,

$$X_2=min\{X_1A_k: k=1,2,\ldots,n-2 \text{ and } A_k\in V-X_1\}$$

then, choose the nearest city A_l from the last visited city A_k and add with the current route which expressed as

$$A_i\leftrightarrow A_j\leftrightarrow A_k\leftrightarrow A_l\ .$$

The set of the route is,

$$X_3=min\{X_2A_l: l=1,2,\ldots,n-3 \text{ and } A_l\in V-X_2\}.$$

Similarly taking every city, return to the initial edge where a city isn't connected (suppose A_i) and the route expressed as

$$A_i\leftrightarrow A_j\leftrightarrow A_k\leftrightarrow A_l\leftrightarrow...\leftrightarrow A_z\leftrightarrow A_i \text{ and}$$

the set of the route is,

$$X_{n-1} = min\{X_{n-2}A_z: z = 1,2, \dots, n-(n-1) \text{ and } A_z \in V - X_{n-2}\}$$

In addition, for more visualization, a flowchart of the improved NNA is shown in Fig. 1.

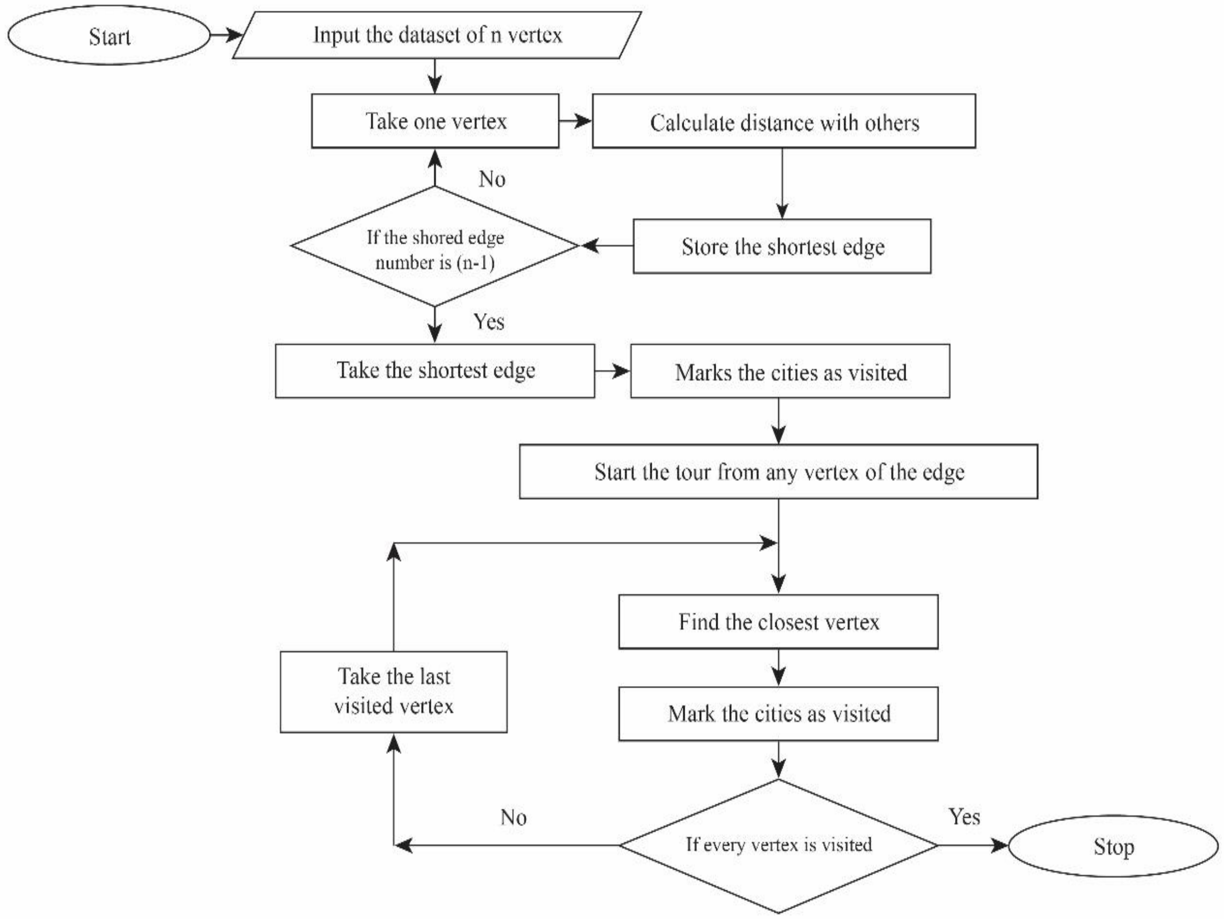

Fig. 1 Flowchart of the proposed improved nearest neighbor search algorithm for TSP

The improved nearest neighbor search algorithm can be explained by the following step by step procedure:

Step:1. Sort all edges from *n* cities.
Step:2. Select an edge with a shortage distance.
Step:3. From the remaining cities, find the nearest unvisited city and combine it with the existing edge.
Step:4. Make a note of the most recent city visited.
Step:5. Find the closest city to the most recent city visited.
Step:6. Add the closest city to the tour and mark as visited.
Step:7. Is there any city that has not yet been visited? If you responded yes, go to step 5.
Step:8. Return to the first chosen edge's starting vertex

5 Results and Discussion

In this particular section, a series of simulations were conducted on various datasets to assess and compare the performance of of the improved NNA to that of the basic NNA. In order to fulfil the simulation objectives, a collection of real-world symmetric Travelling Salesman Problem (TSP) datasets from TSPLIB is taken into consideration. Consider 20 benchmark symmetric TSP datasets with dimensions ranging from 52 to 2103. The dataset name is assigned a number value that corresponds to its dimension. As an example, the alphanumeric identifier "berlin52" represents the numerical value assigned to a specific node consisting of 52 geographical places inside the city of Berlin. Once the datasets have been gathered, it is necessary to compute a symmetric distance matrix in which the diagonal members are set to zero. The distance matrix provides a measure of the distance between the nodes. The evaluation of basic NNA included the computation of the best, worst, and average outcomes, as well as the measurement of the time taken to run the procedure across all datasets. In the improved NNA, each individual test case inside the simulation is executed autonomously, taking into consideration the size of the dataset. In contrast, it should be noted that in the simulation, every test case is executed autonomously, resulting in a twofold increase in the dataset lengths for the basic NNA. Both the basic NNA and improved NNA are implemented using MATLAB R2021a. The simulations are conducted on a computer system equipped with a CORE i5 processor operating at a frequency of 1.80 GHz and 4 GB of RAM.

The simulation findings and subsequent analysis including 20 benchmark datasets have been subjected to testing, comparing the performance of both the basic NNA and improved NNA. Table 1 illustrates the performance comparison between the basic NNA and improved NNA for 20 benchmark datasets. The first column in the table provides a description of the dataset names. The second column provides information pertaining to the quantity of cities. The third column describes the best-known optimal solution. After that, the fourth column describes the optimal solution, execution time of the CPU (in seconds), and error (%) for an improved NNA. The best, average, and worst results, the execution time of the CPU (in seconds), and the error rate (%) for the average and best of each dataset for basic NNA are described in the last column. Here, datasets are also arranged in an ascending order of nodes.

The formula for finding error of improved NNA is

$$\text{Error}\ (\%) = \frac{\text{result of improved NNA} - \text{optimum}}{\text{optimum}}$$

and formula we use for finding error of best and average solution of basic NNA are

$$\text{Error}_{\text{best}}\ (\%) = \frac{\text{best result of NNA} - \text{optimum}}{\text{optimum}}$$

$$\text{Error}_{\text{avg}}\ (\%) = \frac{\text{averge result of NNA} - \text{optimum}}{\text{optimum}}$$

Table 1 Performance comparison between basic NNA and improved NNA

Datasets	**Nodes**	**Optimum Solution**	**Improved NNA**			**Basic NNA**					
			Best	Time(s)	Error (%)	Best	Average	Worst	Time(s)	$\text{Error}_{\text{best}}$ (%)	$\text{Error}_{\text{avg}}$ (%)
berlin52	52	7542	9161	0.01368	21.4664	8149	9396	10188	0.03394	8.04823	24.583
rat99	99	1211	1577	0.01020	30.2229	1507	1695	1911	0.07070	24.4426	39.969
kroC100	100	20749	25519	0.00994	22.9890	26043	27925	30014	0.06900	25.5145	34.587
lin105	105	14379	17363	0.01073	20.7524	19759	21221	23448	0.12903	37.4157	47.582
pr107	107	44303	47233	0.01757	6.61354	46563	53181	60539	0.08233	5.10124	20.032
pr124	124	59030	69066	0.01107	17.0015	67302	75851	84709	0.10606	14.0131	28.496
ch130	130	6110	7341	0.01750	20.1472	7461	7988	8894	0.08022	22.1119	30.734
pr152	152	73682	85243	0.01570	15.6903	86665	94459	107039	0.08970	17.6201	28.192
u159	159	42080	55200	0.02709	31.1787	54509	60038	63711	0.19008	29.5369	42.678
rat195	195	2323	2624	0.03069	12.9573	2751	3023	3277	0.13011	18.4245	30.134
d198	198	15780	18485	0.01764	17.1419	18233	22085	24076	0.17593	15.5449	39.956
kroA200	200	29368	36824	0.01874	25.3881	35161	38291	42451	0.12714	19.7255	30.384
ts225	225	126645	149243	0.07770	17.8435	146769	160600	177560	0.31578	15.8908	26.811
pr264	264	49135	57663	0.02865	17.3562	56947	60446	65021	0.20568	15.8995	23.022
lin318	318	42029	52883	0.04197	25.8250	53621	56250	60102	0.33150	27.5805	33.831
fl417	417	11861	14773	0.05673	24.5510	14603	16323	17539	0.63161	23.1178	37.610
rat575	575	6773	8100	0.10071	19.5924	8345	8774	9245	1.69813	23.2090	29.547
p654	654	34643	43492	0.11859	25.5433	43457	49486	54001	2.27642	25.4426	42.845
fl1400	1400	20127	26461	0.87500	31.4701	26854	28935	31599	30.2443	33.4226	43.761
d2103	2103	80529	88547	5.34190	9.95666	86554	93753	99944	249.528	7.48176	16.424

In Table 1, we show the error (%) comparison between the improved NNA and the basic NNA with the best-known solution. The error (%) of the best result in improved NNA is lower than the average in all 20 cities listed above, and the worst result is in basic NNA. For example, the dataset "rat99" represents the 99 nodes of this city. By using the improved NNA, the optimal is 1577, and the average result of that dataset is 1695 for the basic NNA. The error in improved NNA is 30.2229%, whereas the error in basic NNA is 24.4426% and 39.969% for the best and average results, respectively. Again, for "lin318," using our improved NNA, the optimal solution is 52883. Using the basic NNA, the average result is 56328. The error in improved NNA is 20.7524%, whereas the error in basic NNA is 37.4256% and 47.582% for the best and average results, respectively. Even for the higher number of cities, the same characteristics hold. For example, the dataset "d2103" denotes the number of nodes as 2103. This is a huge number of nodes. By using an improved NNA, the optimal solution for that dataset is 88547. Using the basic NNA, the average result is 93753. The error in improved NNA is 9.95666%, whereas the error in basic NNA is 7.48176% and 16.424% for the best and average results, respectively.

Similarly, for all other datasets. The fourth and fifth columns of Table 1 show a comparison of the computational time between improved NNA and basic NNA for any random dataset. The required time for execution of the improved NNA is less than the basic NNA. For example, using improved NNA, the time of execution of "kroC100" is 0.009948 s, and for basic NNA, it is 0.069040s. Also, by using improved NNA, the time of execution of the dataset "ch130" is 0.017507s, and for basic NNA, it is 0.080252s. Even for the higher number of cities, the same characteristics hold. For dataset ‘fl1400’, the execution time is 0.875745s for improved NNA and 30.244633s for basic NNA. Improved NNA, on the other hand, outperforms basic NNA in terms of computational time. According to the simulation results, improved NNA outperforms both the average and the worst results of basic NNA in terms of values and computational time.

Even with respect to the best-known solution of datasets, the error (%) of some cities in improved NNA is less than the error (%) of the best result in basic NNA. In improved NNA, the optimal solution of 8 datasets provides a better result than the best result of basic NNA. For the dataset "kroC100," the optimal solution is 25519, whereas the best solution for the basic NNA is 26043. For this dataset, the error in the improved NNA is 22.9890%, whereas the error in the basic NNA is 25.5145% for the best result with respect to the best-known solutions to the dataset. Again for "rat195", the optimal solution for improved NNA is 8100, where the best solution for basic NNA is 8345. For this dataset, the error in the improved NNA is 12.9573%, whereas the error in the basic NNA is 18.4245%. Likewise for the other datasets. Therefore, the improved NNA provides better results than the basic NNA, both in the aspect of values and of computational time and reduces error. In Fig. 2 the bar chart shows the error (%) comparison between the improved NNA and the basic NNA with respect to the best-known solutions of 20 symmetric datasets. The colors blue, orange, and yellow represent the best solution error for improved NNA, the best solution error for basic NNA, and the best solution error for basic NNA, respectively.

The bar chart (Fig. 3) shows the error (%) comparison between improved NNA and basic NNA for the 8 best symmetric datasets, which is best against basic NNA. For further visualization, Fig. 4 graphically represents the difference between the improved NNA and the basic NNA of the Best 8 dataset. There are two figures for each dataset in Fig. 4: one for improved NNA and another for basic NNA. The route to an optimal solution is shown in the two figures. Comparing table, graph, and bar charts, it is demonstrated that the improved NNA outperforms the basic NNA in terms of solution quality as well as computational time.

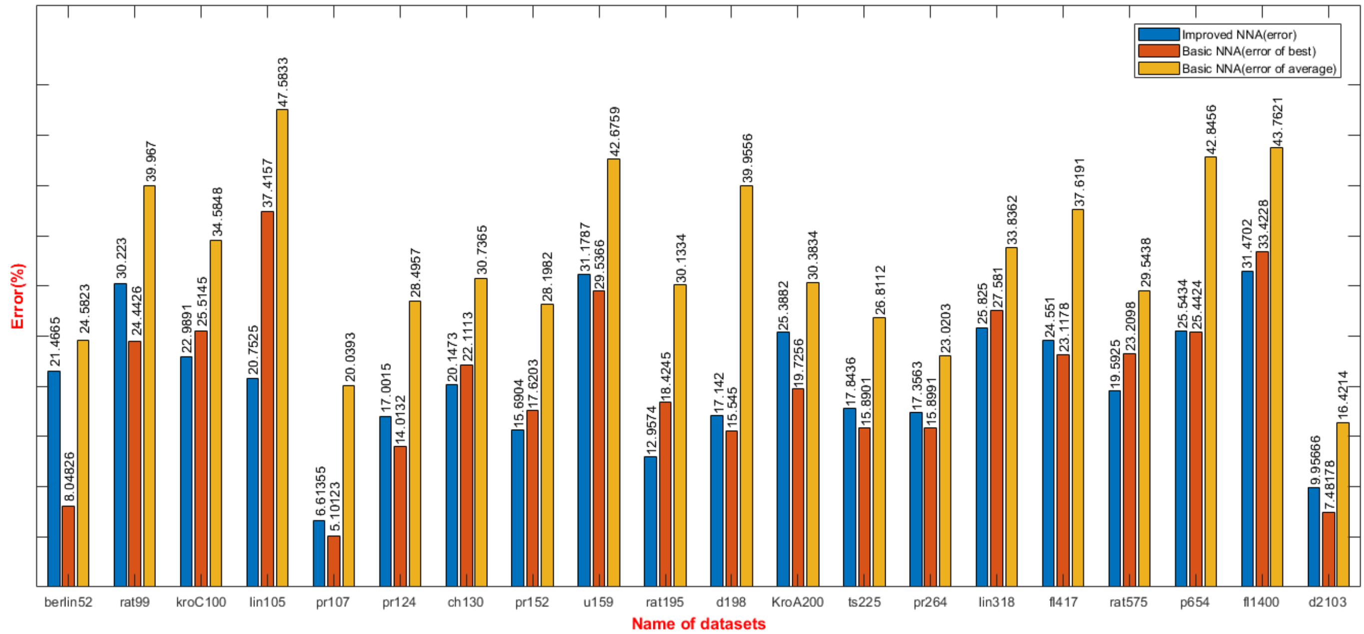

Fig. 2 Error (%) comparison bar charts for the best solution of improved NNA and the average and best solution of basic NNA with respect to the best-known solution for 20 benchmark STSP datasets.

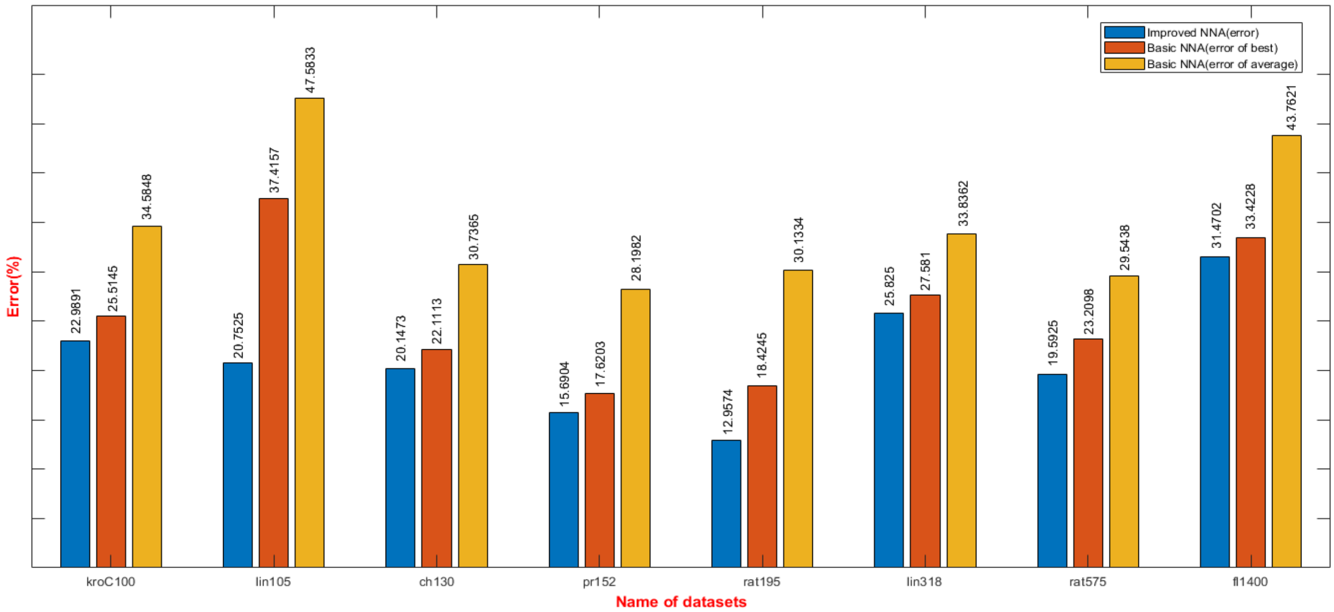

Fig. 3 Error comparison bar charts of improved NNA and basic NNA for best 8 benchmark STSP datasets.

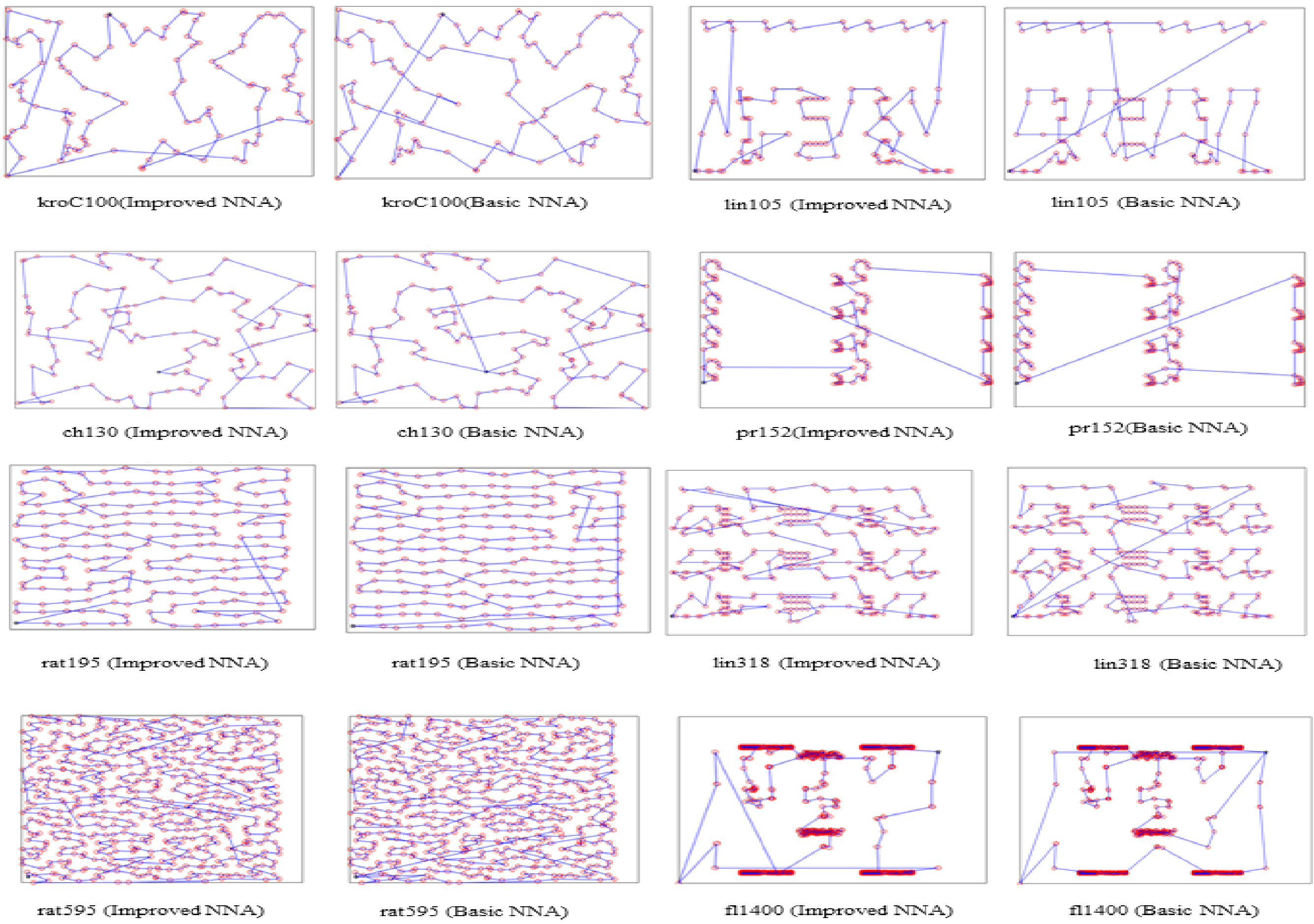

Fig. 4 Obtained optimum route for 8 datasets both of improved NNA and basic NNA

6 Conclusions

The present study improved the basic NNA for solving symmetric TSP. It compared improved NNA with basic NNA because both algorithms are route construction algorithms. However, the main difference between them is that the improved NNA is deterministic, i.e., the results produced by this algorithm are same at every single run. On the other hand, the basic NNA is probabilistic, i.e., this algorithm generates different results at every single run. All datasets have been subjected to comprehensive testing. The simulation findings and subsequent analysis demonstrate that the improved NNA yields superior outcomes compared to the basic NNA. It has been discovered that when the initial solution is selected randomly, the improved NNA outperforms and exhibits more efficiency compared to the basic NNA. Based on the aforementioned datasets, simulation design, and environmental conditions, it can be inferred that improved NNA yields superior outcomes with reduced time consumption. In subsequent analyses, the improved NNA will be juxtaposed with other route construction algorithms. Furthermore, it is possible to develop a hybrid method by integrating the improved NNA with other route construction algorithms. As a result, it will achieving superior outcomes compared to an improved NNA.

References

[1] Rahman, M.A. and Parvez, H., 2021. Repetitive nearest neighbor based simulated annealing search optimization algorithm for traveling salesman problem. *Open Access Library Journal*, *8*(6), pp.1-17.

[2] Applegate, D., Bixby, R., Cook, W. and Chvátal, V., 1998. On the solution of traveling salesman problems.

[3] Dantzig, G., Fulkerson, R. and Johnson, S., 1954. Solution of a large-scale traveling-salesman problem. *Journal of the Operations Research Society of America*, 2(4), pp.393-410.

[4] Deng, W., Chen, R., He, B., Liu, Y., Yin, L. and Guo, J., 2012. A novel two-stage hybrid swarm intelligence optimization algorithm and application. *Soft Computing*, *16*, pp.1707-1722.

[5] Hore, S., Chatterjee, A. and Dewanji, A., 2018. Improving variable neighborhood search to solve the traveling salesman problem. *Applied Soft Computing*, *68*, pp.83-91.

[6] Matai, R., Singh, S.P. and Mittal, M.L., 2010. Traveling salesman problem: an overview of applications, formulations, and solution approaches. *Traveling Salesman Problem, Theory and Applications*, *1*(1), pp.1-25.

[7] Naser, H., Awad, W.S. and El-Alfy, E.S.M., 2019. A multi-matching approximation algorithm for Symmetric Traveling Salesman Problem. *Journal of Intelligent & Fuzzy Systems*, *36*(3), pp.2285-2295.

[8] Halim, A.H. and Ismail, I., 2019. Combinatorial optimization: comparison of heuristic algorithms in

travelling salesman problem. *Archives of Computational Methods in Engineering*, *26*, pp.367-380.

[9] Bentley, J.J., 1992. Fast algorithms for geometric traveling salesman problems. *ORSA Journal on Computing*, 4(4), pp.387-411.

[10] Klug, N., Chauhan, A., V, V. and Ragala, R., 2019. k-RNN: Extending NN-heuristics for the TSP. *Mobile Networks and Applications*, *24,* pp.1210-1213.

[11] Bakar, S.A. and Ibrahim, M., 2017, August. Optimal solution for travelling salesman problem using heuristic shortest path algorithm with imprecise arc length. In *AIP Conference Proceedings*, *1870*(1). AIP Publishing.

[12] Lin, S. and Kernighan, B.W., 1973. An effective heuristic algorithm for the traveling-salesman problem. *Operations Research*, *21*(2), pp.498-516.

[13] Chen, Y. and Zhang, P., 2006. Optimized annealing of traveling salesman problem from the nth-nearest-neighbor distribution. *Physica A: Statistical Mechanics and Its Applications*, *371*(2), pp.627-632.

[14] Raya, L., Saud, S.N., Shariff, S.H. and Bakar, K.N.A., 2020. Exploring the performance of the improved nearest-neighbor algorithms for solving the euclidean travelling salesman problem. *Advances in Natural and Applied Sciences*, *14*(2), pp.10-19.

[15] Rosenkrantz, D.J., Stearns, R.E. and Lewis, II, P.M., 1977. An analysis of several heuristics for the traveling salesman problem. *SIAM Journal on Computing*, *6*(3), pp.563-581.

[16] Sahin, M., 2023. Solving TSP by using combinatorial Bees algorithm with nearest neighbor method. *Neural Computing and Applications*, *35*(2), pp.1863-1879.

[17] Pop, P.C., Cosma, O., Sabo, C. and Sitar, C.P., 2023. A comprehensive survey on the generalized traveling salesman problem. *European Journal of Operational Research*, *314*(3), pp.819-835.

[18] Gutin, G., Yeo, A. and Zverovitch, A., 2002. Exponential neighborhoods and domination analysis for the TSP. In *The Traveling Salesman Problem and Its Variations* (pp. 223-256). Boston, MA: Springer US.

This page is left intentionally blank

Journal of Engineering Advancements (JEA)

DOI: https://doi.org/10.38032/jea

Indexed by:

Volume 05 Issue 01

DOI: https://doi.org/10.38032/jea.2024.01

Published by: SciEn Publishing Group

Website: www.scienpg.com